CrossMark

JM PAPERS

Global instability and mode selection in flow fields around rectangular prisms

Zhanbiao Zhang[1]**, Ahsan Kareem**[2]**, Fuyou Xu**[1,†] **and Hongyi Jiang**[3,4]

[1]School of Civil Engineering, Dalian University of Technology, Dalian 116024, PR China

[2]NatHaz Modeling Laboratory, University of Notre Dame, Notre Dame, IN 46556, USA

[3]Ocean College, Zhejiang University, Zhoushan 316021, PR China

[4]School of Engineering, The University of Western Australia, 35 Stirling Highway, Perth, WA 6009, Australia

Large-eddy simulations of the unsteady flows around rectangular prisms with chord-to-depth ratios (B/D) ranging from 3 to 12 are carried out at a Reynolds number of 1000. A particular focus of the study is the physical mechanisms governing the global instability of the flow. The coherent structures and velocity spectra reveal that large-scale leading-edge vortices (L vortices) are formed by the coalescence of Kelvin–Helmholtz rollers. Based on dynamic mode decomposition, the interactions between the L vortex and the trailing-edge vortex (T vortex) at different B/D values are revealed. It is found that the phase difference between the L and T vortices is the critical factor promoting a stepwise increase in the Strouhal number with increasing B/D. According to the phase analysis, there are two types of pressure feedback-loop mechanisms maintaining the self-sustained oscillations. When $B/D = 4$–5, the feedback loop covers the separation region, and the global instability is controlled by the impinging shear-layer instability. When $B/D = 3$ and 6–12, the feedback loop covers the entire chord, and the global instability is controlled by the impinging leading-edge vortex shedding instability. Self-sustained oscillations of the shear layer still exist after a splitter plate is placed in the near wake, indicating that the T vortex shedding is not essential in triggering the global instability. Nevertheless, with the participation of the T vortex, the primary instability mode may be reselected due to the upper and lower limits of the shedding frequency imposed by the T vortex.

Key words: vortex shedding, vortex interactions, separated flows

† Email address for correspondence: fuyouxu@hotmail.com

1. Introduction

Flow around a flat rectangular prism is characterized by very significant flow separation at the sharp leading edges, unsteady flow reattachment on the afterbody (typically refers to the body part downstream of the flow separation points) and trailing-edge Kármán-type vortex shedding. The Kármán-type vortex shedding is the main source of the vortex-induced vibrations of structures. Although an afterbody is not essential for the occurrence of vortex-induced vibration according to Zhao, Hourigan & Thompson (2018), the unsteady flow reattachment on the afterbody may play an important role in the vortex-induced vibration. Thus, the global features and underlying mechanisms of the flows around rectangular prisms have led to extensive investigation.

The prism chord-to-depth ratio (B/D) is a critical parameter that shapes these flow characteristics, where B and D denote the dimensions parallel and perpendicular to the incoming flow, respectively. According to Parker & Welsh (1983), the separated shear layers are intermittently or permanently reattached to the afterbody when $B/D > 3.2$. Nakamura, Ohya & Tsuruta (1991) studied the vortex shedding behaviour in the range of $3 \leq B/D \leq 16$ at a Reynolds number ($Re = UD/\nu$, where U denotes the free-stream velocity, ν denotes the kinematic viscosity) of 1000. The Strouhal number (St) based on B and U is nearly constant and is equal to 0.6 for $B/D = 3$–5. With further increase in B/D, it increases stepwise to values that are approximately equal to integral multiples of 0.6. With the aid of a smoke-wire, they found that St was closely related to the number of large-scale vortices on the prism's lateral faces, which was later verified in their numerical studies (Ohya *et al.* 1992). Nakamura *et al.* (1991) attributed the formation of the large-scale vortices to the impingement of the separated shear layers on the sharp trailing-edge corners and thus called the mechanism the impinging shear-layer (ISL) instability. The concept of ISL instability is usually used to characterize the self-sustained oscillations of flow past a cavity. For cavity flows, researchers have found that the global instability is caused by the upstream propagation of the pressure pulse generated by the impingement of the large-scale vortices in the shear layer on the trailing edge, as was reviewed by Rockwell & Naudascher (1978). This pressure pulse in turn enhances the unsteadiness of the leading-edge shear layer and the large-scale vortex shedding.

However, global instability still exists in large-B/D cases where the separated shear layer does not directly impinge on the trailing edge. In addition, Stokes & Welsh (1986) found that no significant change occurred after replacing square trailing-edge corners with a semi-circle, suggesting that the trailing edge does not need to be sharp to trigger the instability. Thus, Naudascher & Rockwell (1994) later called the global instability the impinging leading-edge vortex (ILEV) instability to emphasize that it is the large-scale vortices shed from the leading-edge shear layer that interact with the trailing edge rather than the shear layer itself. Nguyen, Hargreaves & Owen (2018) studied the mechanism of the vortex-induced vibration of a 5:1 rectangular prism and noted that the vortex-induced vibration is triggered by the motion-induced leading-edge vortex, while the impingement of this vortex on the trailing edge is responsible for the increase in the structural response during the lock-in of the vortex shedding and structural vibration frequencies.

Another significant difference between the flows over a rectangular prism and over a cavity is the participation of the trailing-edge vortex shedding (TEVS) in the former case. Hourigan *et al.* (1993) found that interference occurred between the leading-edge vortices (L vortices) and the trailing-edge vortices (T vortices) by imposing an acoustic perturbation. Furthermore, Hourigan, Thompson & Tan (2001) noted that the TEVS played an important role in the self-sustained oscillations and was responsible for the stepwise progression of the Strouhal number with B/D. This hypothesis of vortex interactions

between the ILEV and TEVS was further confirmed by Mills, Sheridan & Hourigan (2002, 2003) and Tan, Thompson & Hourigan (2004) in flows with transverse perturbations. In particular, Tan *et al.* (2004) pointed out that the narrow-banded instability of the TEVS controlled the stepwise changes in the Strouhal number.

The unsteadiness of the separated shear layer also depends on the Reynolds number. For low *Re*, the separated shear layers are steadily reattached on the prism surface, and regular Kármán-type vortex shedding is formed in the wake. With an increase in *Re*, the shear layers tend to be more unstable and eventually evolve into the ILEV instability in a wide range of *Re*. Okajima (1982) pointed out that this critical *Re* for the transition of the shear layer is dependent on *B/D*. Nakamura *et al.* (1996) studied the Strouhal number for different *B/D* values (*B/D* = 3–16) in the *Re* range of 200–1000 and concluded that the critical *Re* was about 300. By further increasing *Re*, regular vortex shedding is weakened by the increasing three-dimensional (3-D) turbulence after reattachment. Nakamura *et al.* (1991) found that the stepwise variation of *St* with *B/D* disappeared at *Re* = 2000. Nevertheless, Mills *et al.* (2003) showed that it could be reproduced by adding a small transverse perturbation to the flow, suggesting that the underlying mechanism of the ILEV instability still exists at higher Reynolds numbers. Recently, Duan *et al.* (2020) experimentally investigated the flow over a flat plate with elliptical leading and trailing edges at *Re* = 8100. As the 3-D turbulence effect was minimized without sharp edges, regular vortex shedding was detected in their study.

Although it is widely accepted that the flow around a rectangular prism is governed by the ISL or ILEV instabilities, sometimes accompanied by TEVS, there remain some significant questions to be answered. For example, the complex interaction behaviour between ILEV and TEVS, the exact form of the pressure feedback loop controlling the global instability for different *B/D*, the range and source of the preferred shedding frequency of TEVS, the underlying mechanisms of the mode switches at certain *B/D* values and the stepwise increase manner of *St* have not been fully explored.

The particle image velocimetry technique and computational fluid dynamics simulations greatly facilitate the exploration of the evolution of vortex structures through flow visualization. To identify the coherent structures in the flow fields from time-resolved data, a common practice is to perform a modal decomposition. The dynamic mode decomposition (DMD) method proposed by Schmid (2010) provides a means to decompose the original flow into a series of modes, with each mode containing a single characteristic frequency and growth rate. Thus, it is suitable for the identification of the spatiotemporal coherent structures in periodic flows and has been used in the analyses of cavity flows (Seena & Sung 2011; Guéniat, Pastur & Lusseyran 2014), backward-facing step flows (Sampath & Chakravarthy 2014) and flows around cylinders (Thompson *et al.* 2014; Zhang, Liu & Wang 2014; Stankiewicz *et al.* 2016; Li *et al.* 2019) and cantilever beams (Cesur *et al.* 2014). More recently, the dynamic pressure field over a finite-height prism immersed in a boundary layer flow has been examined using DMD (Luo & Kareem 2021).

In the present study, the large-eddy simulation method and the DMD analysis technique are used to extract coherent structures in the ILEV and TEVS and to uncover the pressure feedback-loop mechanism of the global instability and the fundamental mechanism for the stepwise variation of *St* with *B/D*. The Reynolds number of this study is 1000, under which the leading-edge vortices are shed from the unstable shear layer but without being submerged by the downstream turbulence caused by the 3-D modulations. The *B/D* ranges from 3 to 12, covering four stages (0.6–2.4) of the Strouhal number (Nakamura *et al.* 1991). In addition, two special cases are included to explore the roles played by the TEVS in the self-sustained oscillations of the shear layers by separating the ILEV and TEVS.

955 A19-3

The rest of this paper is organized in the following manner. Section 2 details the numerical model, simulation cases, mesh arrangement and mesh convergence check. Section 3 introduces the DMD algorithm and illustrates the two-dimensionality of the global instability. The sources and evolution of the ILEV and TEVS and their interaction behaviours are studied in § 4 with $B/D = 5$ as an example. In § 5, the pressure feedback-loop mechanisms for the global instability at different B/D values are investigated. The roles played by the TEVS in the global instability and the stepwise increase in the Strouhal number are revealed in § 6, followed by the main conclusions in § 7.

2. Numerical model

2.1. *Governing equations of flow*

The 3-D incompressible, unsteady flow around the prism is modelled by the filtered Navier–Stokes equations:

$$\frac{\partial \bar{u}_i}{\partial x_i} = 0, \qquad (2.1)$$

$$\frac{\partial \bar{u}_i}{\partial t} + \frac{\partial \bar{u}_i \bar{u}_j}{\partial x_j} = -\frac{1}{\rho}\frac{\partial \bar{p}}{\partial x_i} + \frac{\partial}{\partial x_j}\left(\nu \frac{\partial \bar{u}_i}{\partial x_j} - \tau_{ij}\right), \qquad (2.2)$$

where the overbar stands for the spatial filter operation; x_i denotes the ith Cartesian coordinate, u_i denotes the velocity component in the direction x_i, t is time, p is pressure, ρ is fluid density, ν is kinematic viscosity and $\tau_{ij} = \overline{u_i u_j} - \bar{u}_i \bar{u}_j$ is the subgrid-scale stress and is modelled by the dynamic k-equation model developed by Yoshizawa (1986).

The governing equations are solved by the open-source finite-volume code OpenFOAM. The implicit second-order backward differentiation scheme is adopted for temporal integration. The so-called Gauss limited linear scheme, a second-order-accurate bounded total variational diminishing scheme, is used for spatial discretization of the convection term, while the second-order central difference scheme is used for the diffusion term. The gradient term is evaluated using the least-squares method. The velocity–pressure coupling is achieved by the pressure-implicit with splitting of operators (PISO) algorithm with two correctors in each time step. The convergence criterion for p is 1×10^{-6}.

2.2. *Simulation cases*

Figure 1 shows a schematic diagram of the numerical cases simulated in this study. First, rectangular prisms with B/D values ranging from 3 to 12, with a unit interval, are used to investigate the variations of the flow characteristics with B/D. In particular, the critical value of B/D at which the flow pattern jumps from the first mode ($St = 0.6$) to the second mode ($St = 1.2$) is explored. Furthermore, two special configurations are presented to separate the ILEV and TEVS. Case II is characterized by a splitter plate in the wake to eliminate the TEVS. In Case III, the leading-edge separated shear layer is removed, and only TEVS is expected to occur. This is equivalent to a prism of infinite width, where the interactions between the ILEV and TEVS are negligible and the TEVS can be analysed separately.

2.3. *Computational domain, boundary conditions and mesh arrangement*

Figure 2 shows a schematic view of the computational domain and boundary conditions for the regular prisms (i.e. Case I in figure 1). The distances from the prism centre to

955 A19-4
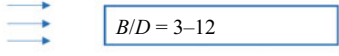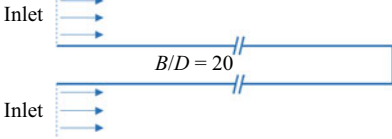
Case	Vortex shedding type	Sketch map
I	ILEV+TEVS	$B/D = 3\text{–}12$
II	ILEV	$B/D = 6$ Splitter $(5D)$
III	TEVS	Inlet $B/D = 20$ Inlet

Figure 1. Simulation cases. Case I represents regular rectangular prisms. Case II and Case III are designed to separate the ILEV and TEVS.
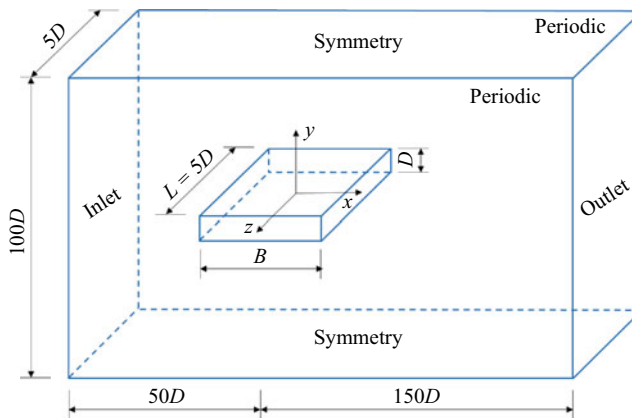

Figure 2. Computational domain and boundary conditions for Case I.

the inlet and outlet boundary are $50D$ and $150D$, respectively. The transverse dimension of the computational domain is $100D$, resulting in a blockage ratio of 1%. The spanwise dimension, i.e. the prism length L, is set as $5D$, which is determined based on a comparison with $10D$ in § 2.4.

A uniform flow velocity U is specified at the inlet boundary. At the outlet boundary, the Dirichlet boundary condition (zero value) is used for pressure, while the Neumann boundary condition (zero gradient) is used for velocity. The top and bottom boundaries are set as symmetry, while the front and back boundaries are periodic. No-slip wall boundary is applied to the prism surface. Similar strategies are adopted for Cases II and III and not given herein for brevity.

The mesh in the x–y plane is hybrid, with 20 layers of structured grids around the prism and unstructured quadrilateral grids in the rest of the domain, as shown in figure 3 for $B/D = 5$. To solve the small-scale vortex structures around the prism, the grids in the near-wall and near-wake regions are refined. The grid size within the structured region is $0.02D \times 0.02D$, leading to a unit grid aspect ratio and an average y^+ about 1.0 and a maximum y^+ about 3.0 during simulations. The grid spacing gradually increases away
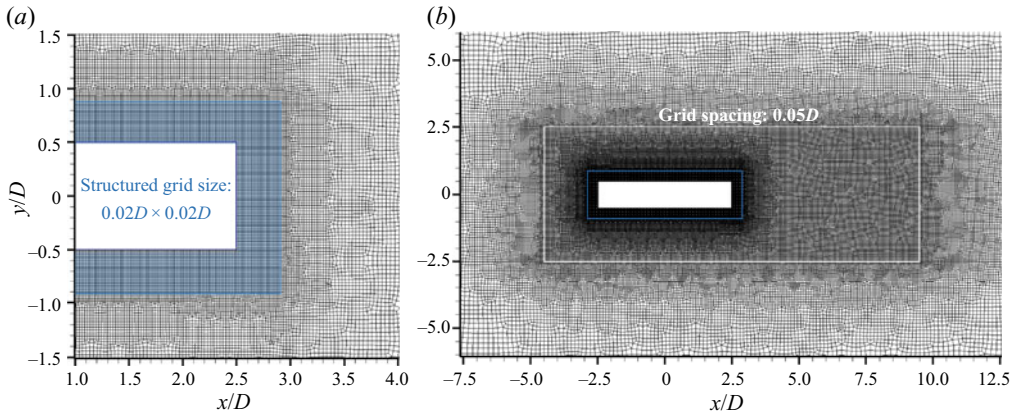
Figure 3. Mesh arrangement around the prism with $B/D = 5$: (*a*) 20 layers of structured mesh in body vicinity; (*b*) unstructured mesh in the rest area.

from the wall. In figure 3(*b*), the grid size at the perimeter of the white rectangle (7*D* downstream of the prism's rear face and 2*D* from other faces) is 0.05*D*.

The 3-D mesh is obtained by extruding the two-dimensional (2-D) mesh in the *x–y* plane along the spanwise direction with a uniform step size (δz). In the present study, $\delta = 0.05D$ is adopted following a dependence study on δz (see § 2.4). This leads to 100 layers in the spanwise direction for the 3-D mesh. The total cell number for regular prisms varies from 9.6 million ($B/D = 3$) to 15.1 million ($B/D = 12$). For Cases II and III, there are 15.7 million and 10.5 million cells, respectively.

2.4. *Mesh resolution and spanwise domain size*

It is known that mesh resolution, in both the *x–y* plane and the spanwise direction, and the spanwise domain size may have significant influences on the simulated flow around a rectangular prism (Bruno, Coste & Fransos 2012; Zhang & Xu 2020). In the present study, a mesh dependence study is performed. Based on the reference mesh introduced in § 2.3, which is labelled as Case (i), three variations are examined:

(ii) The *L* value is increased from 5*D* to 10*D*.
(iii) The δz value is decreased from 0.05*D* to 0.025*D*.
(iv) The δx and δy values in the inner zone are decreased from 0.02*D* to 0.01*D*.

Detailed mesh arrangements for the four cases are listed in table 1. For Cases (i)–(iii), the non-dimensional time step size $\delta t^* = \delta t \cdot U/D$ is set as 0.01, where δt is the physical time step size. While for Case (iv), δt^* is 0.005. The maximum Courant number is below 1.2. Each simulation lasts 600 non-dimensional time units, while the data in the first 300 time units are discarded to exclude the initial undeveloped flow period.

Table 1 lists the Strouhal number, the time-averaged drag coefficient (C_D-*avg*) and the standard deviation of lift coefficient (C_L-*std*) obtained from different arrangements. The Strouhal number is defined as

$$St = \frac{fB}{U}, \tag{2.3}$$

Case	L/D	$\delta z/D$	$\delta x/D \times \delta y/D$	St	C_D-avg		C_L-std	
					Value	Deviation from Case (i)	Value	Deviation from Case (i)
(i)	5	0.05	0.02×0.02	0.576	0.992	0	0.865	0
(ii)	10	0.05	0.02×0.02	0.575	0.989	-0.3%	0.846	-2.2%
(iii)	5	0.025	0.02×0.02	0.575	0.993	0.1%	0.823	-4.8%
(iv)	5	0.05	0.01×0.01	0.576	0.971	-2.1%	0.816	-5.6%

Table 1. Simulated aerodynamic force coefficients and St with different mesh arrangements.
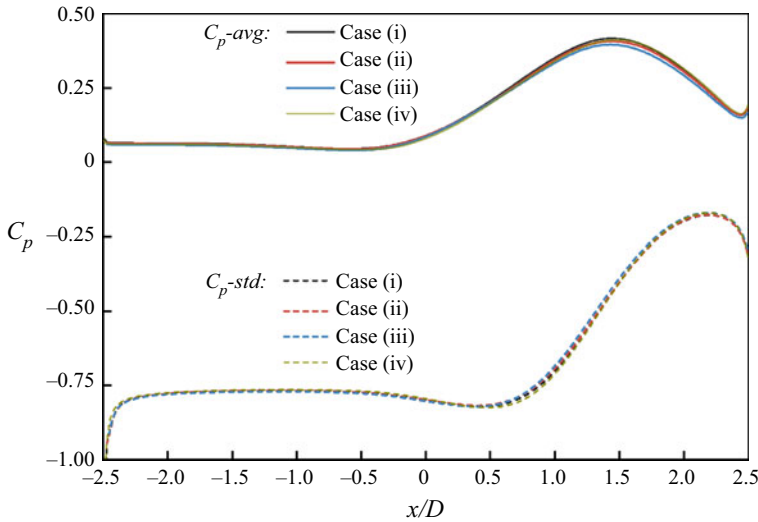
Figure 4. Spanwise- and side-averaged pressure coefficients on the lateral faces with different mesh arrangements.

where f is the peak frequency of the unsteady lift coefficient and is calculated by the fast Fourier transform (FFT) technique. The drag and lift coefficients are defined as

$$C_D = \frac{F_D}{0.5\rho U^2 DL}, \tag{2.4a}$$

$$C_L = \frac{F_L}{0.5\rho U^2 DL}, \tag{2.4b}$$

where F_D and F_L are the unsteady drag and lift forces, respectively. It can be found that the aerodynamic force coefficients calculated from different cases are fairly close. The error of C_L-std is relatively large, while the key parameter of this study, i.e. St, stays almost constant.

The time-averaged value (C_p-avg) and standard deviation (C_p-std) of the surface pressure coefficients are plotted in figure 4. Data are averaged along the spanwise direction and between the top and bottom surfaces. In general, the influences of L and δz are very limited. For C_p-avg, the four curves almost coincide with each other. For C_p-std, the deviations of the peak value from Case (i) are within 5%.
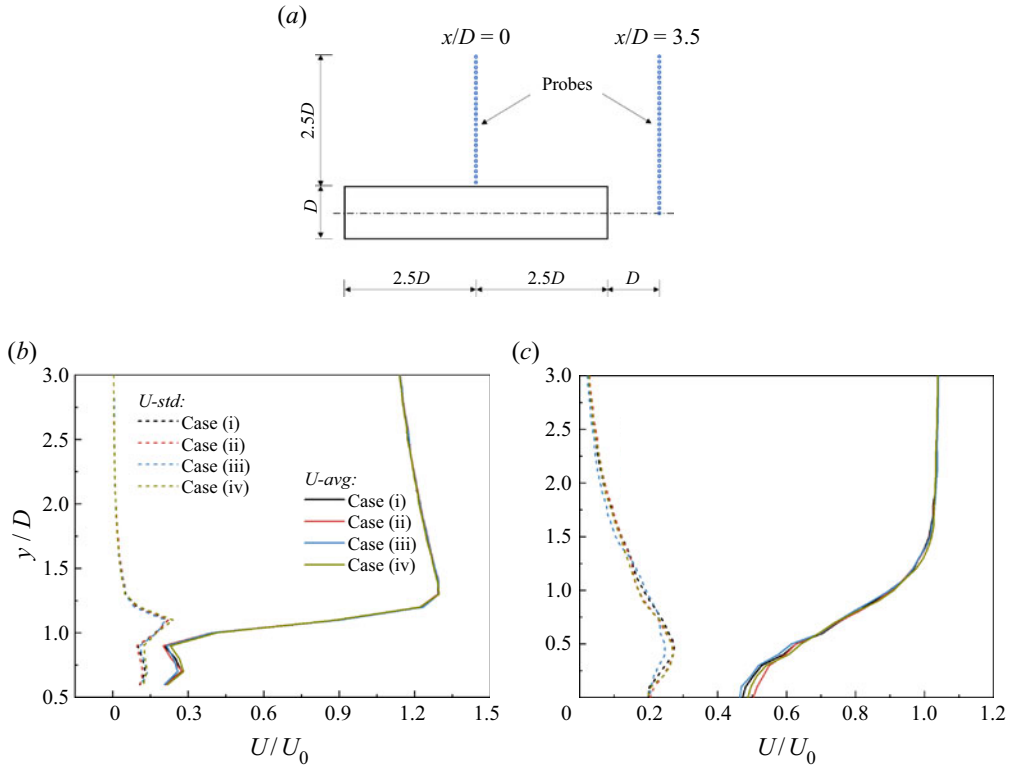
Figure 5. Midspan velocity profiles with different mesh arrangements: (*a*) probe locations; (*b*) $x/D = 0$; (*c*) $x/D = 3.5$.

To check the mesh convergence of velocity fields around the prism, the time-varying velocities at two columns of probes at $x/D = 0$ and 3.5 are monitored, as shown in figure 5(*a*). The spanwise location of the probes is $z = 0$ (midspan). Figures 5(*b*) and 5(*c*) display the time-averaged (*U-avg*) and standard deviations (*U-std*) of the velocity profile along $x/D = 0$ and 3.5, respectively. For both regions, different mesh arrangements give close estimates of *U-avg* and *U-std*. Thus, it can be concluded that the meshing parameters for Case(i), i.e. $L = 5D$ and $\delta z = 0.05D$, can give a nearly converged estimation of the main flow features and are therefore adopted for the following simulations.

3. Dynamic mode decomposition

3.1. *The DMD algorithm*

For a linear system, $x^{n+1} = Ax^n$, if the eigenvalues and eigenvectors of the coefficient matrix A are determined, one can obtain the main evolution characteristics of the system. In the present study, the DMD method proposed by Schmid (2010) is used for the eigenvalue decomposition of matrix A.

First, by consecutively sampling the system at an interval of δt, the data can be arranged into a snapshot matrix:

$$X = (x(t_1), x(t_2), \ldots, x(t_n)), \tag{3.1}$$

where each column denotes an instantaneous snapshot of the system. For an unsteady pressure field, X is expressed as follows:

$$X = \begin{pmatrix} p_{node_1}(t_1) & p_{node_1}(t_2) & \cdots & p_{node_1}(t_n) \\ p_{node_2}(t_1) & p_{node_2}(t_2) & \cdots & p_{node_2}(t_n) \\ \vdots & \vdots & \ddots & \vdots \\ p_{node_k}(t_1) & p_{node_k}(t_2) & \cdots & p_{node_k}(t_n) \end{pmatrix}, \quad (3.2)$$

where $node_1$–$node_k$ denote the spatial dimension of the flow fields, i.e. the number of degrees of freedom, while t_1–t_n denote the temporal dimension, i.e. the sampling length. Similarly, one can construct another matrix:

$$Y = (x(t_2), x(t_3), \ldots, x(t_{n+1})), \quad (3.3)$$

where $Y = AX$.

Second, the singular value decomposition or the proper orthogonal decomposition (POD) of X is computed as follows:

$$X = USV^*, \quad (3.4)$$

where U contains the POD modes of the system and S represents the energetic importance of each mode. To reduce the computational cost, only the first r order modes are retained to approximate the original flow fields: $Ur = U(1:k, 1:r)$, $Sr = S(1:r, 1:r)$ and $Vr = V(1:n, 1:r)$. In this study, it is found that the first 100 order POD modes contain more than 95% of the energy of the original flow fields, and the DMD spectra calculated based on the first 100 and 200 POD modes are very close. Thus, $r = 100$ is adopted for computational efficiency.

Third, $X = Ur Sr Vr^*$ is substituted into $Y = AX$, and then A can be expressed as follows:

$$A = Y Vr Sr^{-1} Ur^*. \quad (3.5)$$

Although matrix A is obtained, it has an order of $k \times k$, which means that a direct eigenvalue decomposition of A is extremely difficult for large-scale systems. An alternative approach is to reduce the order by projecting A onto Ur:

$$\tilde{A} = Ur^* A Ur = Ur^*(Y Vr Sr^{-1} Ur^*) Ur = Ur^* Y Vr Sr^{-1}. \quad (3.6)$$

Note that the order of $\tilde{A}$ is only $r \times r$, and performing eigenvalue decomposition for $\tilde{A}$ is very efficient:

$$[W, \Lambda] = \text{eig}(\tilde{A}). \quad (3.7)$$

Here A and $\tilde{A}$ are similar matrices, and thus they share the same eigenvalues: $\lambda_i = \text{diag}(\Lambda)$. The eigenvalues of the DMD modes can then be calculated by $\omega_i = \log(\lambda_i)/\delta t$. The real part of ω_i denotes the growth rate of the ith mode, while the imaginary part denotes the oscillating frequency. For the eigenvectors, i.e. the DMD modes, Tu *et al.* (2013) pointed out that there are two kinds of definitions. The first is the projected DMD mode:

$$\hat{\Phi} = UW. \quad (3.8)$$

The second is the exact DMD mode:

$$\Phi = Y V \Lambda^{-1} W. \quad (3.9)$$

In this study, the exact DMD mode is adopted for the following analyses. Like the eigenvalues, the DMD modes are also in complex form. For a specific mode

$\boldsymbol{\varphi}_i = (x_1 + \mathrm{i}y_1, x_2 + \mathrm{i}y_2, \ldots, x_k + \mathrm{i}y_k)^{\mathrm{T}}$, the phase angle at each spatial point can be calculated by

$$\theta_i^k = \arctan\left(\frac{y_k}{x_k}\right). \tag{3.10}$$

Based on the distribution of the phase angle in the entire domain, a more direct understanding of the fluctuating behaviour of the instability mode can be obtained.

Finally, based on the eigenvalues and eigenvectors, the flow evolution corresponding to a specific DMD mode can be reconstructed:

$$\boldsymbol{x}_i(t) = \boldsymbol{\varphi}_i^{\mathrm{T}} \boldsymbol{x}(t_1)\, \mathrm{e}^{\omega_i(t-t_1)} \boldsymbol{\varphi}_i = \psi_i(t)\boldsymbol{\varphi}_i, \tag{3.11}$$

where $\psi_i(t) = \boldsymbol{\varphi}_i^{\mathrm{T}} \boldsymbol{x}(t_1)\, \mathrm{e}^{\omega_i(t-t_1)}$ represents the temporal coefficient of mode $\boldsymbol{\varphi}_i$.

Although the derivation above is based on a linear system, Rowley *et al.* (2009), Tu *et al.* (2013) and Mezić (2013) pointed out that the DMD algorithm is also applicable to nonlinear systems by revealing its relationship with the Koopman operator. To obtain satisfactory results, Schmid (2010) noted that the sampling frequency should be at least three times the inherent frequency. The DMD algorithm for vector fields, such as the velocity field, is similar to that for a scalar field, with the only exception that each component of the vector should be treated as an individual degree of freedom and then arranged into an integral snapshot matrix.

Unlike the POD approach where the modes are arranged in the order of energy contents, there is no objective ranking of the eigenvalues in the DMD approach; thus it is difficult to determine the most physically relevant modes. In this study, the main modes which are related to the flow global instability are identified through the following guidelines. First, the global instability is expected to be caused by the self-sustained oscillations of the shear layer and periodic shedding of the TEVS, and thus the growth rate of concerned modes should be close to zero, provided that the sampling length is large enough. Second, the spectrum of the lift force provides a direct reference for the selection of the DMD mode by comparing the frequencies. Third, the DMD modes directly obtained by (3.9) are first normalized based on the magnitude, and the time-varying coefficient $\psi(t)$ of each mode can be calculated, then the modes are reordered by their 2-norm of $\psi(t)$. The mode with higher $\|\psi(t)\|$ represents higher energy and is more likely to be the dominant mode of the global instability.

3.2. *Two-dimensionality of DMD mode of global instability*

The sampling length and frequency play significant roles in the decomposition accuracy. Thus, a large number of snapshots are usually needed to be stored when constructing matrix $\boldsymbol{X}$. If the target is the 3-D flow fields, it will require a large amount of memory and computational time to perform the DMD analysis, which may be prohibitive in most cases. The emphasis of this study is to examine the streamwise evolution of the vortices dominating the global instability. If the 3-D fluctuations can be expressed by a 2-D slice in the *x–y* plane, the computational effort will be significantly reduced. Thus, in this section, the effectiveness of the 2-D DMD for extracting the global instability structures is examined through the DMD mode of the pressure coefficients on the top surface of the prism.

Two prisms, i.e. $B/D = 5$ and 6, are examined, which correspond to scenarios where one and two vortices exist on each lateral side of the prism, respectively, according to Nakamura *et al.* (1991). There are in total 40 000 snapshots for each case, and the time interval between two consecutive snapshots is 0.01, corresponding to about 46 and 70
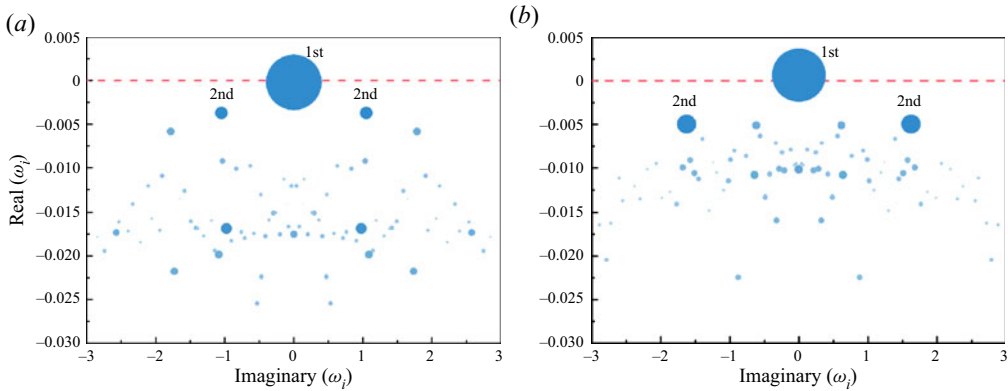
Figure 6. Dynamic mode decomposition spectra of the surface pressure for: (*a*) $B/D = 5$ and (*b*) $B/D = 6$. The areas of the circles are related to the energy of the modes.

vortex shedding periods, respectively. The spectra of the DMD eigenvalues are depicted in figure 6, where the abscissa and ordinate represent the imaginary and real parts of ω_i, respectively. The areas of the circles are scaled by $||\psi(t)||$.

From the spectra, the relatively stable (real $(\omega_i) \approx 0$) and high-energetic modes can be easily identified. The real and imaginary parts of the first mode marked in the figure are close to zero, representing zero growth and no oscillations. Thus, the first mode represents the time-averaged pressure field. Apart from the first mode, the second modes have the second largest area and are closest to the real $(\omega_i) = 0$ axis. The values of St calculated by the eigenvalues of the second modes for the two prisms are 0.571 and 1.062, respectively. The results calculated using the FFT of C_L are 0.576 and 1.064, respectively, suggesting that the second modes are essentially the global instability modes. For the sake of brevity, the global instability mode is referred to as the St mode hereafter. The spectra are symmetric about the imaginary $(\omega_i) = 0$, i.e. a pair of conjugate modes exists for each non-zero frequency. Figure 7 shows the pressure distributions of the first mode and the real and imaginary parts of the second mode for the two prisms. It should be noted that figure 7 only shows the shape of a specific DMD mode, i.e. $\boldsymbol{\varphi}_i$ in (3.11). The absolute value of the pressure fluctuations corresponding to a specific mode $\boldsymbol{\varphi}_i$ can be obtained by multiplying its time-varying coefficient $\psi_i(t)$. The imaginary part has a $\pi/2$ phase lag relative to the real part. Thus, it can be inferred that the global instability mode has a travelling-wave form, consistent with the physical background of the vortex shedding behaviour associated with the global instability.

As shown in figure 7, the first and second modes both show strong correlations in the spanwise direction, suggesting that the surface pressure fluctuations are mainly governed by the streamwise evolution of the vortices.

In addition, DMD is performed on the 3-D velocity fields to further check the 2-D features of the global vortex shedding modes. The vortical structures within the velocity DMD modes are identified based on the iso-surfaces of the Q criteria, as shown in figure 8 for $B/D = 5$ and 6. Here Q is defined as

$$Q = \tfrac{1}{2}(\|\boldsymbol{\Omega}\|^2 - \|\boldsymbol{S}\|^2), \tag{3.12}$$

where S and Ω are the symmetric and antisymmetric components of the velocity gradient tensor, respectively. Parameter Q represents the local balance between shear strain rate and vorticity magnitude. Positive Q corresponds to the rotational motion of the flow, and higher
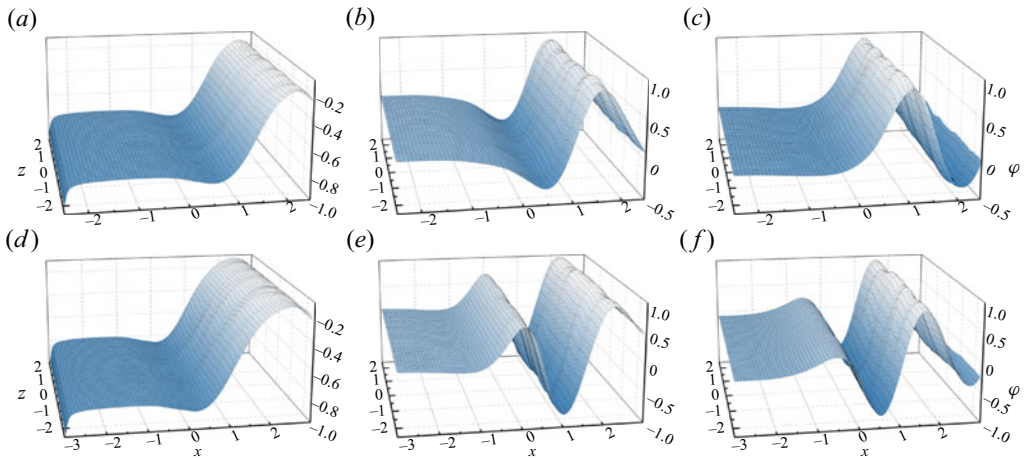
955 A19-11

Figure 7. Dynamic mode decomposition modes of surface pressure: (*a*) $B/D = 5$, first mode; (*b*) $B/D = 5$, second mode, real part; (*c*) $B/D = 5$, second mode, imaginary part; (*d*) $B/D = 6$, first mode; (*e*) $B/D = 6$, second mode, real part; (*f*) $B/D = 6$, second mode, imaginary part.
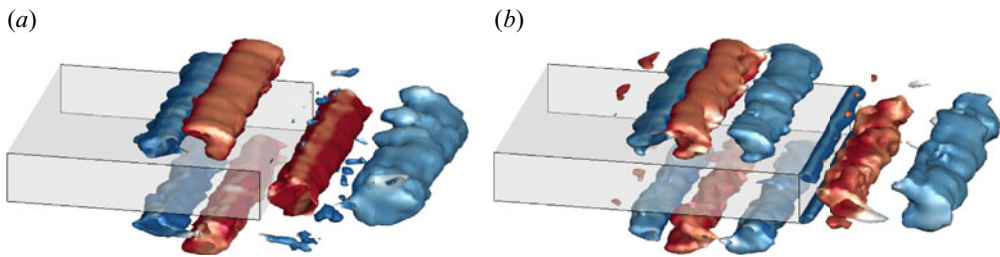

Figure 8. Global instability modes identified from the 3-D velocity fields: (*a*) $B/D = 5$; (*b*) $B/D = 6$. Vortical structures are demonstrated by iso-surfaces of $Q = 0.2(U/D)^2$, blue tubes have a clockwise direction of rotation and red tubes have an anti-clockwise direction of rotation.

Q means higher vortex intensity. These Q criteria are considered to be more appropriate than the vorticity criteria for extracting vortex structures, especially in the near-wall region where the shear effect in the flow is predominant.

From figure 8, several spanwise vortex tubes are observed on the lateral sides of and in the wake of the prisms, indicating that the global vortex shedding is almost synchronous along the spanwise direction. This permits us to use the 2-D flow fields in the *x*–*y* plane for the following DMD analyses to avoid high computational efforts. In the present study, the spanwise-averaged flow is used for the 2-D DMD analysis because it contains more averaged information than a slice in the 3-D flow. Detailed discussion on the evolution of the vortical structures of the DMD modes is given in § 4.2.

4. Flow characteristics for $B/D = 5$

Before exploring the flow characteristics at different *B/D* values, it is useful to investigate the flow characteristics at a specific *B/D* to obtain a preliminary understanding of the pattern of the global instability. In this section, the main focus is placed on the behaviour of the unsteady flow around the prism with $B/D = 5$. First, the instantaneous vortex structure in the original flow is extracted to study the evolution of leading- and trailing-edge vortices.
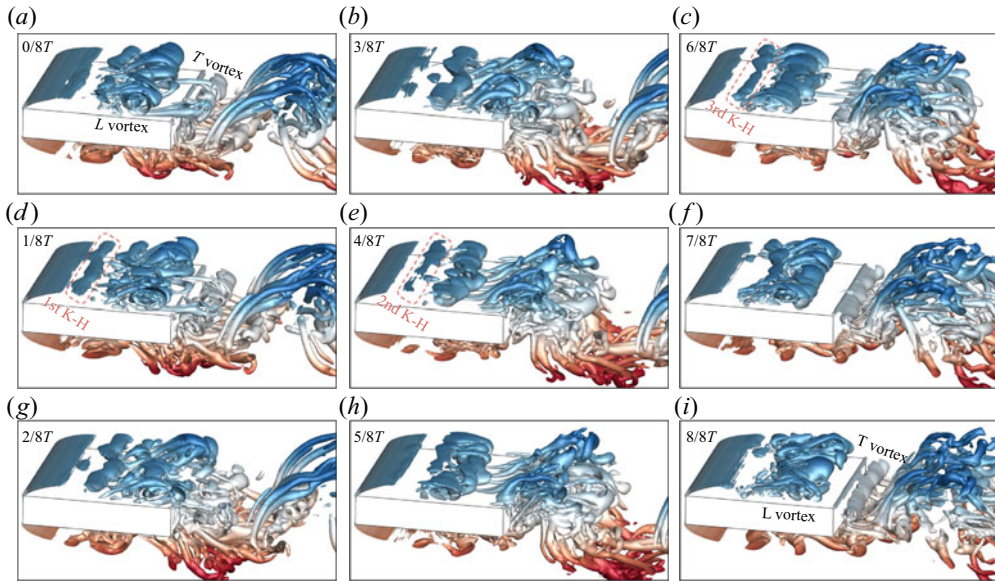
955 A19-12

Figure 9. (a–i) Evolution of coherent structures during one vortex shedding cycle for $B/D = 5$, demonstrated by iso-surfaces of $Q = 1.0(U/D)^2$, coloured based on the y coordinate.

In particular, the source of the large-scale leading-edge vortex is explored. Then DMD is applied to the spanwise-averaged velocity field to reveal the interactions between the ILEV and TEVS. Finally, the phase of the fluctuations is extracted from the pressure DMD mode to obtain a preliminary understanding of the feedback loop of the self-sustained oscillations.

4.1. *Formation of leading- and trailing-edge vortices*

The instantaneous coherent structures of the 3-D flow fields during one vortex shedding cycle are extracted based on the Q iso-surfaces, as shown in figure 9.

At $t = 0$, a large-scale leading-edge vortex and a Kármán-like trailing-edge vortex appear above the top face and behind the leeward face, respectively. For brevity, in the text below, the leading- and trailing-edge vortices are referred to as the L and T vortices, respectively. At $t = T/8$, accompanied by the shedding of the L and T vortices, a small-scale spanwise vortex structure emerges in the leading-edge shear layer, which is caused by the Kelvin–Helmholtz (KH) instability. During the whole period, there are three KH rollers on the upper side, which are shed from the leading-edge shear layer at $t/T = 1/8$, $4/8$ and $6/8$. The downstream convection velocity of the first KH roller gradually decreases after being shed, promoting its subsequent coalescence with the second and third KH rollers at $t = 5T/8$ and T, respectively. The merger of the KH rollers in the leading-edge separation bubble was also detected by Sasaki & Kiya (1991), Hwang, Sung & Hyun (2000) and Chaurasia & Thompson (2011) for a blunt flat plate at relatively low Reynolds numbers ($Re < 800$). In particular, Sasaki & Kiya (1991) noted that the number of the merging KH rollers increased with Re. The merged large-scale vortex structure at $t = T$ is actually the new L vortex and then propagates through the trailing edge over $t/T \sim 1/4$ to $3/4$ in the next cycle. For the remaining half-cycle from $3T/4$ to $T + T/4$, a relatively small T vortex is formed near the upper trailing edge without the influence of the large L vortex. During shedding, convection and coalescence, the KH rollers experience notable
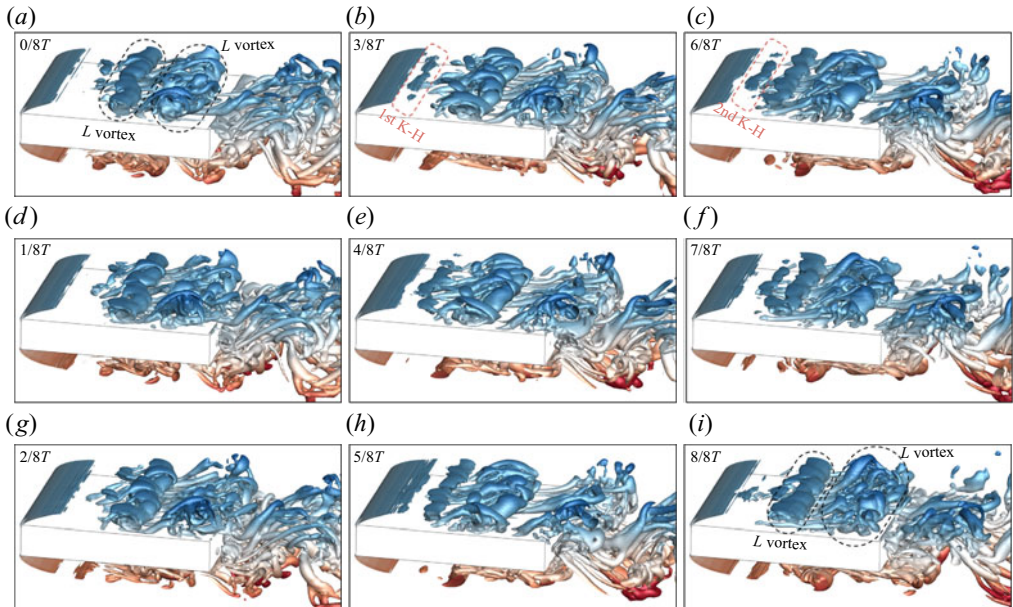
Figure 10. (*a–i*) Evolution of coherent structures during one vortex shedding cycle for $B/D = 6$, demonstrated by iso-surfaces of $Q = 1.0(U/D)^2$, coloured based on the y coordinate.
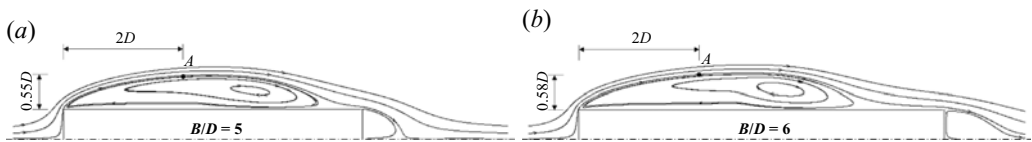

Figure 11. Locations of sampling probe A in the shear layer for (*a*) $B/D = 5$ and (*b*) $B/D = 6$.

spanwise modulations. Furthermore, the L vortex is stretched to 3-D hairpin-like vortices when it flows past the trailing edge due to the strong shear effect near the wall.

Figure 10 shows the instantaneous coherent structures during one shedding cycle for $B/D = 6$. In contrast to the case of $B/D = 5$ shown in figure 9, every two KH rollers merge together and form the ILEV for $B/D = 6$, suggesting that the number of shedding KH rollers in one cycle is related to B/D. In addition, two large-scale vortices appear over the chord in figure 10, indicating a transition of the global instability from Mode 1 to Mode 2. However, the Kármán-type vortex shedding from the trailing edge is almost invisible. The underlying mechanism for such a mode transition is discussed in detail in § 5.2.

To better study the relationship between the KH instability and global instability, we defined a probe A in the upper shear layer and sampled the fluctuating velocity at that point. The probe is located at the midspan ($z = 0$) and is $2D$ downstream from the leading edge, as shown in figure 11. The heights of the probe for $B/D = 5$ and $B/D = 6$ are $0.55D$ and $0.58D$, respectively, which correspond to the upper boundary of the mean separation bubble.

Figure 12 shows the spectra of the normalized transverse velocity U_y/U_0 at point A for $B/D = 5$ and 6. To facilitate comparison, the frequency is scaled by D rather than B. Several prominent peaks appear in both cases, including the global instability frequency, f_G, its harmonics, $2f_G$ and $3f_G$, and the KH instability frequency, f_{KH}. Side-band frequencies of
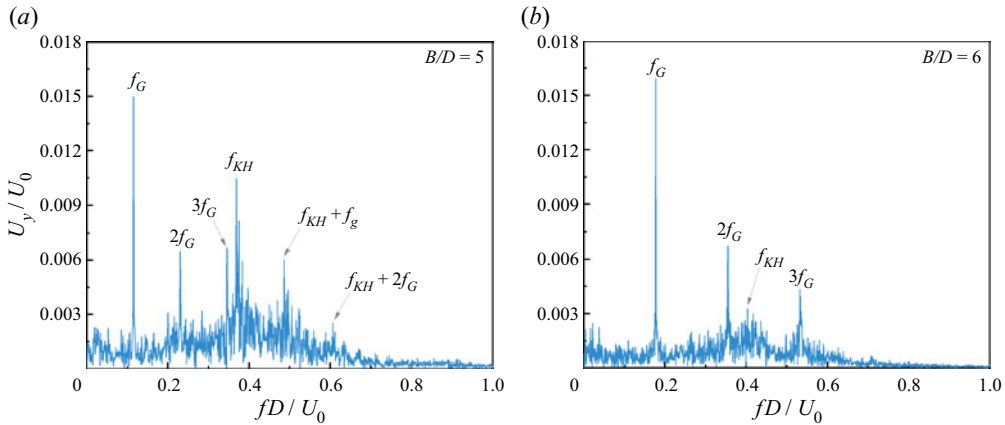
955 A19-14

Figure 12. Spectra of the transverse velocity at point A in the shear layer for (*a*) $B/D = 5$ and (*b*) $B/D = 6$.

$f_{KH} + f_G$ and $f_{KH} + 2f_G$ also appear in the case of $B/D = 5$, which is expected to be caused by the nonlinear interactions between the large-scale vortex structures and the KH rollers. The f_{KH} in the case of $B/D = 5$ is close to $3f_G$, in accordance with the coalescence of every three KH rollers during one shedding cycle of the large-scale vortex observed in figure 9. In contrast, f_{KH} is closer to $2f_G$ for $B/D = 6$. Thus, two KH rollers merge together during one shedding cycle in figure 10. It is worth noting that the f_{KH} values in the two cases are similar (around 0.4), and the decrease for f_{KH}/f_G for $B/D = 6$ is caused by the increase in f_G as a result of the mode transition of the global instability. In figure 12(*b*), the transverse velocity at the frequency of f_{KH} is lower than that in figure 12(*a*). The reason may be that the f_G value for $B/D = 6$ is much higher than that for $B/D = 5$, and the KH rollers are less developed before their merger into a large-scale leading-edge vortex. Thus, the KH instability for $B/D = 6$ is weaker than that for $B/D = 5$.

Figures 9 and 10 show that the subsequent shedding and merging of a certain number of KH rollers in the leading-edge shear layer are the source of the ILEV. How the KH instability, which has a significantly lower fluctuation amplitude in the spectra, forms the large-scale instability of ILEV remains unclear. To determine this, the time histories of U_y/U_0 at probe A at two spanwise locations and their time-frequency spectra computed using the Morlet wavelet transform (Kijewski & Kareem 2003) are presented in figure 13. Several 'packets' of high-frequency fluctuations, which correspond to the KH instability, can be observed. The inset in figure 13(*a*) shows a close-up view of the first 'packet' over $t = 500$–550. The amplitudes of the high-frequency fluctuations in these 'packets' are much larger than those for the primary shedding frequency, indicating that the KH rollers contain a large amount of energy to be transferred to the ILEV. Nevertheless, the high-frequency fluctuations appear only intermittently, making them less apparent in the long-time-averaged velocity spectra and leading to a broad-band peak at f_{KH} in figure 12. It is worth noting that these large-amplitude 'packets' of high-frequency fluctuations exist for all B/D values. Cimarelli, Leonforte & Angeli (2018) studied the relationship between the low-frequency unsteadiness of the separation bubble and the small-scale structures in the shear layer based on direct numerical simulations for a 5:1 rectangular cylinder. They noted that the low-frequency unsteadiness alternatively promotes and suppresses the small-scale motions with a relatively long period of inversion, which further leads to the rising of the 'packets' of high-frequency fluctuations.
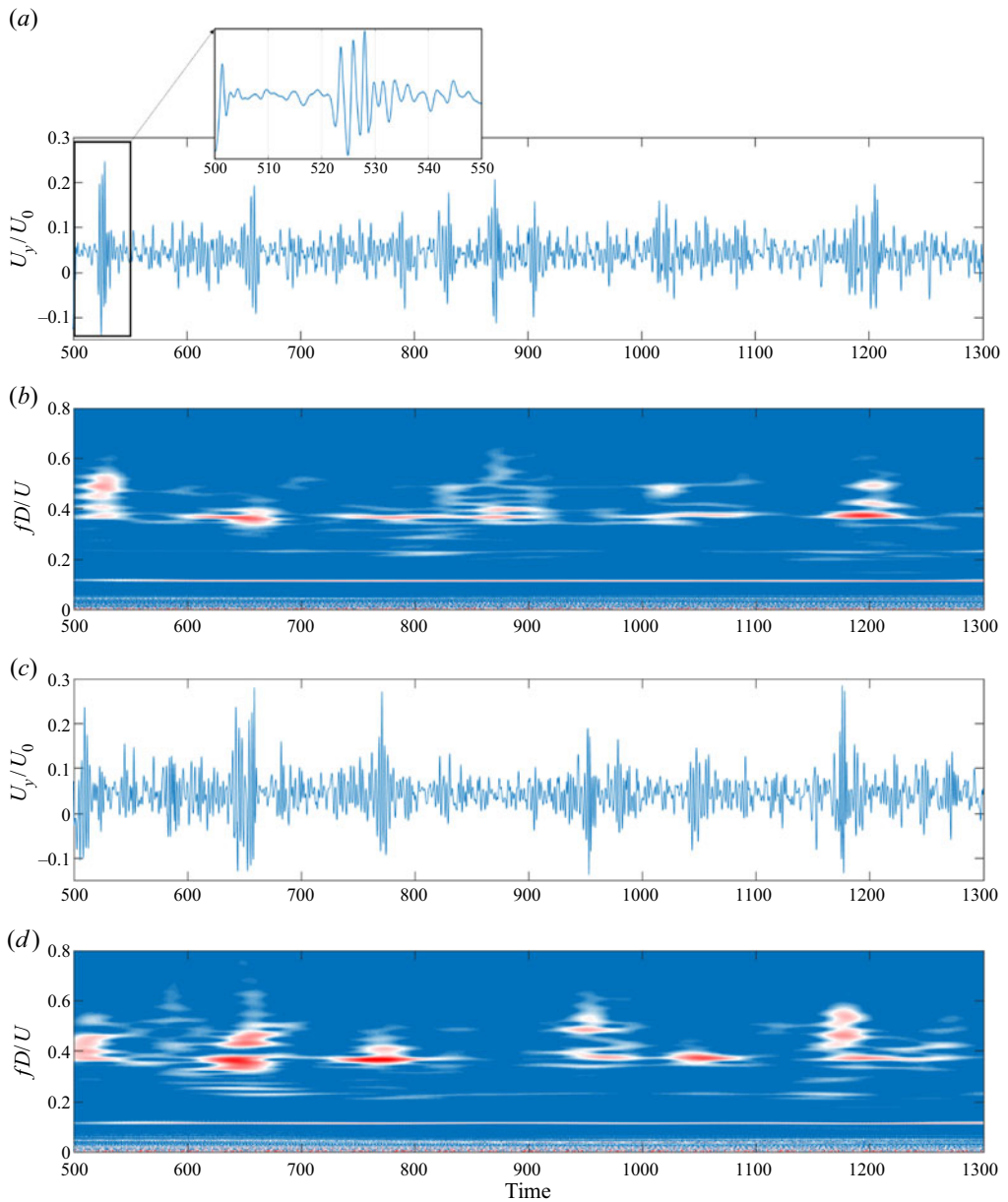
Figure 13. Time histories and time–frequency spectra of the transverse velocity of point A at $z = 0$ (a,b) and $z = -1.5D$ (c,d) for $B/D = 5$.

From figures 13(a) and 13(c), it can be noticed that the amplitudes and locations of the 'packets' of high-frequency fluctuations show significant differences between $z = 0$ and $-1.5D$, suggesting that the KH instabilities at different locations are not enhanced or suppressed simultaneously. In addition, it can be directly observed from figures 9 and 10 that the KH rollers are not fully correlated in the spanwise direction. Thus, it is surmised that the intermittency of KH instability is mainly caused by the 3-D disturbance in the flow on the KH rollers. For the flows over a circular prism, 3-D streamwise structures can

955 A19-16

be detected in the near wake at a much lower *Re*, which have been referred to as Mode B by Williamson (1988). With an increase in *Re*, Prasad & Williamson (1997) pointed out that the temporal changes in the 3-D streamwise structures may disrupt ordered formation of the 2-D shear-layer vortices and thus contribute significantly to the intermittency of shear-layer fluctuations. In particular, they noted that the intermittency of KH instability tends to be significant when *Re* is just above the onset of shear-layer instability, which is close to 1000. Thus, it is believed that the intermittency of K-H instability for a rectangular prism appearing in this study shares some similarities with that for a circular prism. Further studies need to be carried out to explore the behaviour and mechanism of 3-D streamwise structures for rectangular prisms.

4.2. *Interactions between ILEV and TEVS*

To investigate the interactions between the ILEV and TEVS, DMD is performed based on the unsteady spanwise-averaged velocity field. Then, the *Q* field is calculated based on the velocity field corresponding to a specific velocity DMD mode. To perform DMD, 1000 snapshots with a time interval of 0.1 are recorded, corresponding to about 12 vortex shedding periods. The sampling frequency is about 87 times the inherent frequency of global instability, much higher than the minimum requirement proposed in Schmid (2010). Figure 14 shows the evolution of the *St* mode during one vortex shedding period. The *L* and *T* vortices are labelled by their shedding sequences from the trailing edge. The background is coloured by the *Q*-criterion values to demonstrate the vortex intensity distribution for this mode.

It is worth emphasizing that the vortices in the DMD mode are different from the vortex structures of the original flow in figure 9. The two adjacent *L* or *T* vortices in this *St* mode are counter-rotating. The red letters denote clockwise vortices, and the black letters denote anti-clockwise vortices. In addition, the *L* vortices are antisymmetric about the horizontal axis. To illustrate the relationship between the *L* vortices in the original flow and the decomposed flow that correspond to the *St* mode, the original velocity field is divided into the mean field and the fluctuating field, as shown in figure 15. It can be noted that the *St* mode is very similar to the pure fluctuating field for this *Re*. Thus, the fluctuating field is used to illustrate the relationship of the *L* vortices between the original and decomposed flows.

Taking the lower side of the prism as an example, only an anti-clockwise *L* vortex is observed in the original and mean flows, while a pair of counter-rotating vortices are noticed in the fluctuating flow. Supposing that the mean flow is superposed on the fluctuating flow, the clockwise-rotating vortex in the fluctuating flow will be masked (or negated) by the anti-clockwise separation bubble or the near-wall shear effect (in the region downstream the separation bubble) in the mean flow. As a result, only an anti-clockwise vortex is observed on the lower side. Similar conclusions can be drawn for the upper side of the cylinder. Thus, the *L* vortex shedding in the original flow is equivalent to the alternative shedding of the counter-rotating vortex pairs in the *St* mode.

The ILEV, TEVS and their interaction process are recognized through the DMD mode. The process is as follows. (1) At $t = 0$, *L*1 advected from the upstream location arrives at the trailing edge. Meanwhile, *T*1 is formed and begins to shed from the trailing edge. (2) At $t = T/8$, *L*1 and *T*1 begin to merge during their shedding process from the trailing edge. (3) At $t = T/4$, *T*1 is advected away, and a new *T*2 emerges in the near wake. In addition, a new *L*3 appears near the leading edge of each lateral side. (4) Vortex *L*3 moves downstream, and *T*2 continues growing until $t = T/2$, when *L*2 arrives at the trailing edge and *T*2 begins to shed. The above processes form the first half-cycle of the *St* mode,
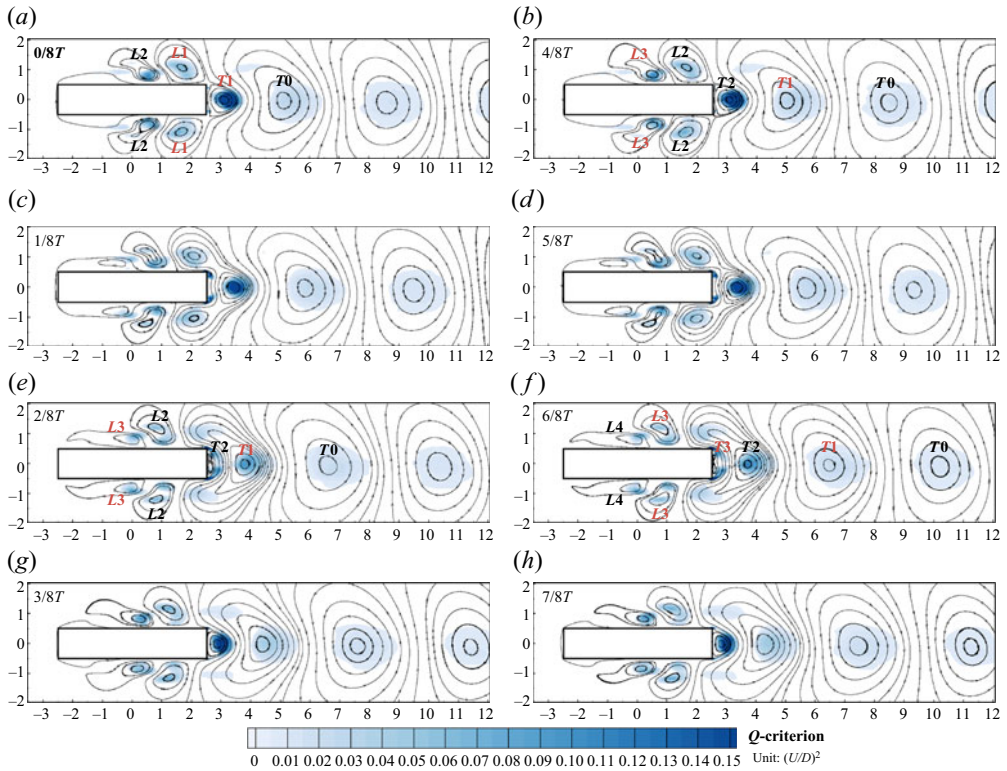
Figure 14. (*a*–*h*) Streamlines and Q contours of the DMD mode at $St = 0.571$ during one shedding cycle for $B/D = 5$.
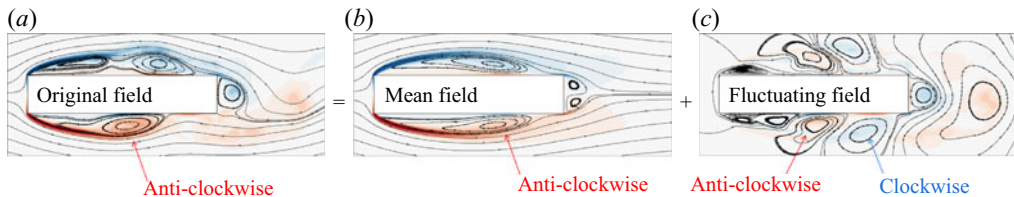

Figure 15. Comparisons of the (*a*) original, (*b*) mean and (*c*) fluctuating velocity fields for $B/D = 5$.

corresponding to the complete shedding and interaction of $L1$ and $T1$. The evolution of the vortices in the second half-cycle is similar to that of the first half-cycle, except that the rotation direction of the shed vortices ($L2$ and $T2$) is opposite to that of the first half-cycle. This shedding and merging behaviours of the L and T vortices at the trailing edge provide direct supporting evidence for the vortex interaction hypothesis suggested by Hourigan *et al.* (1993).

The Q contours mark well the locations of the leading-edge and trailing-edge vortices, while the KH rollers are not present in the St mode. This is due to the frequency-based nature of the DMD technique and the fact that the shedding frequency of the KH rollers is higher than that of the ILEV.
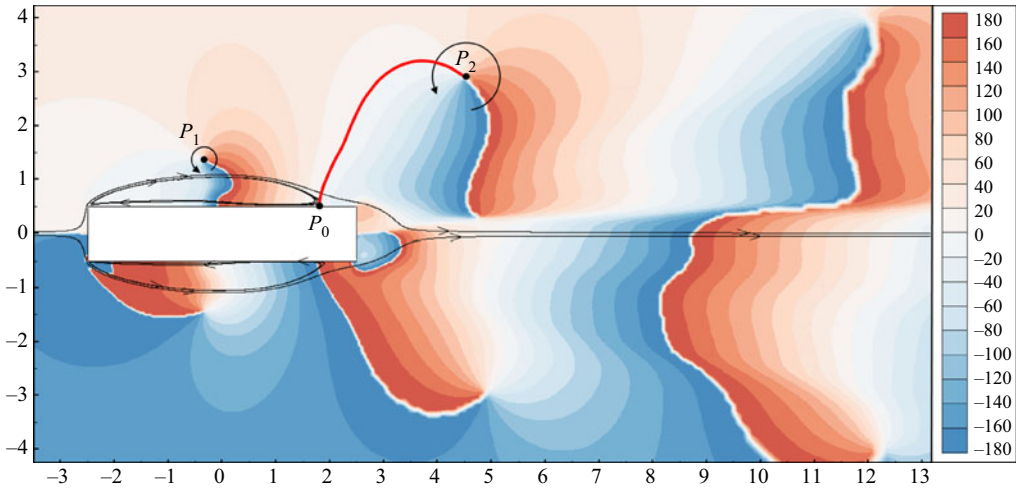
955 A19-18

Figure 16. Phase of pressure fluctuations relative to the upper leading edge in the *St* mode for $B/D = 5$.

4.3. *Pressure phase*

To better understand the relationship between the fluctuations in different regions, the phase angle of the pressure fluctuations at each point in the *St* mode are calculated from the pressure DMD mode using (3.10). For convenience of analysis, the point near the upper leading edge is selected as the reference point. The phase lags of the pressure fluctuations at other points relative to the leading edge are calculated and presented in figure 16. The time-averaged streamlines are also presented in the figure.

Since the *St* mode is antisymmetric, a 180° phase difference between the upper and lower fields exists, and only the upper phase field is discussed here. In the region of $x = -2.5D$ to $-0.5D$, the phase decreases slowly, indicating that the fluctuations in this region are nearly synchronous. A rapid decrease in the phase along the shear layer occurs around $x = 0$, which is considered to be related to the formation of the ILEV. Since the direction perpendicular to the contour lines denotes the propagation direction of the pressure fluctuations, the arc-shaped contour lines around $x = 0$ denote the growth of the *L* vortex in size. Interestingly, there are some special points, denoted by P_1 and P_2, corresponding to the endpoints of the phase contour lines. Surrounding each point, there exists a counter-clockwise propagation of the pressure fluctuations. However, the pressure fluctuations at these points are always zero, representing stagnation points in the pressure field. The distance between the adjacent stagnation points roughly represents the wavelength of the fluctuations.

For the shear-layer instability to be self-sustained, the downstream generating point and upstream receiving point of the pressure pulse in the feedback loop should be in phase. Unexpectedly, the downstream zero-phase point is not at the sharp trailing edge but is at the slightly further upstream point P_0. This means that the pressure feedback-loop mechanism between the leading and trailing edges in the cavity flow is not applicable herein, i.e. the feedback loop does not cover the entire chord length. In addition, the phase of the near-wake region is significantly higher than those at the leading and trailing edges on the same side, suggesting that the TEVS does not directly participate in the feedback-loop mechanism. Therefore, the exact feedback-loop mechanism driving the self-sustained oscillations of the shear layer and the role played by the TEVS in the global instability warrant more in-depth investigation based on a larger range of *B/D* values.
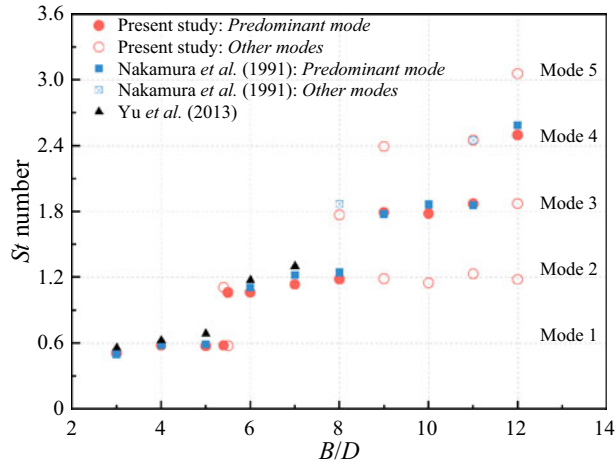
Figure 17. Variation of *St* with *B/D*.

5. Effect of *B/D* on flow characteristics

5.1. *Strouhal number*

The unsteady flow fields around rectangular prisms with *B/D* values ranging from 3 to 12 are simulated. The Strouhal number based on *B* calculated from the spectra of C_L is plotted in figure 17, along with the experimental results from Nakamura *et al.* (1991) and the numerical results from Yu *et al.* (2013). The predominant frequency component (referred to as the main *St* mode below) at a specific *B/D* is marked by a filled circle, while the other frequencies are marked by open circles. Note that only the frequency components whose amplitudes are higher than 10% of the predominant frequency component are plotted. The simulation results show good agreement with the existing results. The results from Yu *et al.* (2013) are slightly higher because *Re* in that study was around 10^5, and Nakamura *et al.* (1991) showed that higher *Re* usually lead to higher shedding frequencies. The stepwise increasing behaviour of the main *St* with *B/D* is captured. Mode 1 to Mode 5 represent the five *St* modes as the *St* value increases from 0.6 to 3.0, with a step size of 0.6.

The experimental results by Nakamura *et al.* (1991) show that when *B/D* = 8 and 11, near the main *St* jump from Mode 2 to Mode 3 and from Mode 3 to Mode 4, respectively, two modes coexist in the system. A similar phenomenon can be observed in the simulation results of this study, but multiple frequencies occur in wider ranges of *B/D*, including the first *St* jump from Mode 1 to Mode 2 within *B/D* = 5.4–5.5 and all the cases with *B/D* ≥ 8. This indicates that the flow near a *St* jump is unstable and the vortex shedding cannot be completely controlled by a specific mode. Thus, the mode jump is more like a process in which lower-order modes gradually disappear while higher-order modes gradually surface, rather than a sudden switch between the two. This can be better understood from the spectra of C_L in figure 18. For example, Mode 3 becomes the primary instability mode when *B/D* ≥ 9 but has already manifested itself in the system when *B/D* = 8.

In general, a larger *B/D* corresponds to more unstable modes and more complicated and distributed frequency contents. In particular, up to four *St* modes are found to coexist in the system (relative amplitude >10%) when *B/D* = 12. It is worth pointing out that the amplitudes of C_L for high-*B/D* cases are significantly smaller than those of low-*B/D* cases. To make figure 18 clearer, the relative amplitude is used for the ordinate, i.e. the amplitudes are scaled by the maximum amplitude for each *B/D* case.
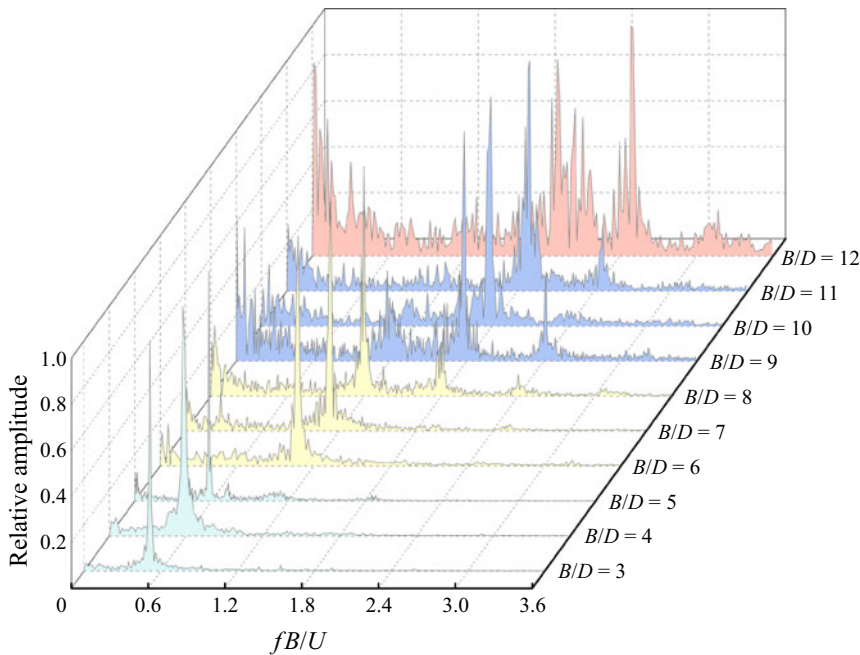
Figure 18. Amplitude spectra of C_L for different B/D values. The amplitudes are scaled by the maximum amplitude for each B/D.

Although low-frequency components seem to be more remarkable for high-B/D cases, their absolute values are still much lower than those of the low-B/D cases.

In figure 17, the modes are classified as the predominant mode and other modes. However, this does not mean that flow is always governed by the predominant mode. Taking $B/D = 9$ as an example, figure 19 shows the time–frequency spectrum of C_L. Mode 3 governs the system most of the time. Within the short periods of $t \sim 900$–1050 and 1700–1900, however, Mode 3 almost disappears, Mode 2 and Mode 4 become the more important modes. Similarly, Mode 4 emerges within $t \sim 800$–1100 and 1500–1900, while it disappears within $t \sim 500$–800 and 1100–1500. This switching behaviour of the primary mode with time can be viewed as a mode competition process, during which each mode is intermittently amplified and suppressed. The DMD modes of Modes 2–4 at $B/D = 9$ are identified and compared in § 5.2.

Similar mode competition phenomena were also detected in Kegerise *et al.* (2004), Murray & Ukeiley (2007), Pastur *et al.* (2008), Lusseyran, Pastur & Letellier (2008) and Guéniat *et al.* (2014) for a cavity flow. It is generally accepted that mode competition or mode switching is a result of the amplitude-modulation effect of the low-frequency fluctuations in the flow fields on the shear-layer oscillation modes (Rossiter modes). The modulation of the low-frequency fluctuations induces two side-band frequencies around the carrier frequency (the mode frequency), making the oscillations exhibit a beating process (Yalla & Kareem 2001). With regard to the physical explanation behind the modulation, Bres & Colonius (2008) claimed that the modulation was caused by the nonlinear interactions between the 3-D centrifugal instability inside the cavity and the oscillating shear layer. Basley *et al.* (2013) found that the 2-D vortex-edge interactions at the impingement and the low-frequency dynamics in the 2-D recirculating flow over
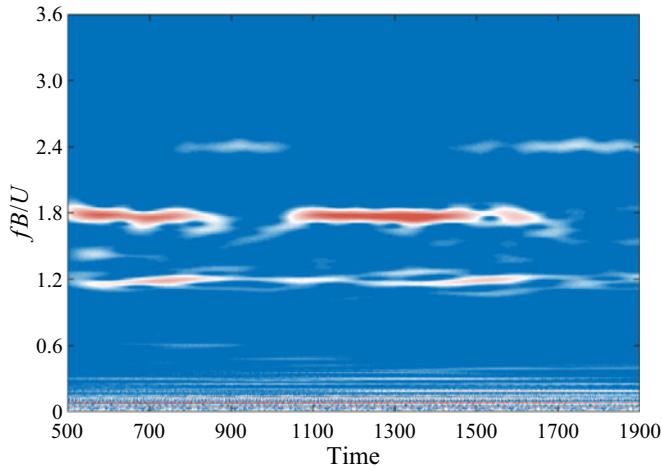
Figure 19. Time–frequency spectrum of C_L at $B/D = 9$.

a very restricted range of width-to-depth ratios were also responsible for the amplitude modulation.

As shown in figure 18, some low-frequency components are evident for $B/D \geq 8$, and each St mode is accompanied by a series of side-band frequencies, indicating that amplitude modulation may also occur in the flow around rectangular prisms. A band-pass filter is further applied to the simulated C_L for $B/D = 9$ to extract the main and side-band frequencies of each mode, i.e. the modulated signal of each mode. The results are shown in figure 20. Under the modulation effect, each mode exhibits strong beating, and the amplification and suppression time intervals are in agreement with figure 19. Although the centrifugal instability in the cavity flow is not observed herein for the separated and reattached flow, the three-dimensionality of the flow is more prominent, especially after reattachment and inside the main separation bubble. Thus, multiple modulations of the St modes may exist concurrently as well as coupling, making the mechanism complicated. As a result, there is no distinct regularity in the beats of the modulated signals.

5.2. *The DMD mode of global instability*

To determine the underlying mechanism that controls which instability modes are selected and enhanced at a specific B/D, the main St mode at each B/D is extracted from the spanwise-averaged velocity field. Figure 21 shows the instantaneous streamlines of the main St mode for different B/D values, and the mode orders are indicated in the top-left corners. Note that for each B/D, figure 21 only shows the mode pattern at the specific instant when a clockwise L vortex just arrives at the trailing edge, i.e. $t = 0$ in figure 14, instead of the entire evolution process during one shedding cycle. Some key findings are summarized as follows:

(1) For $B/D = 3$–5, 6–8, 9–11 and 12, there are two, four, six and eight L vortices on each side of the prism, respectively. Since a pair of counter-rotating L vortices in the DMD mode correspond to one L vortex in the original flow, the number of L vortices for each B/D value predicted in the present study is consistent with the experimental observations of Nakamura *et al.* (1991). Every mode jump brings about an additional pair of L vortices on each side and the total number of pairs is consistent with the
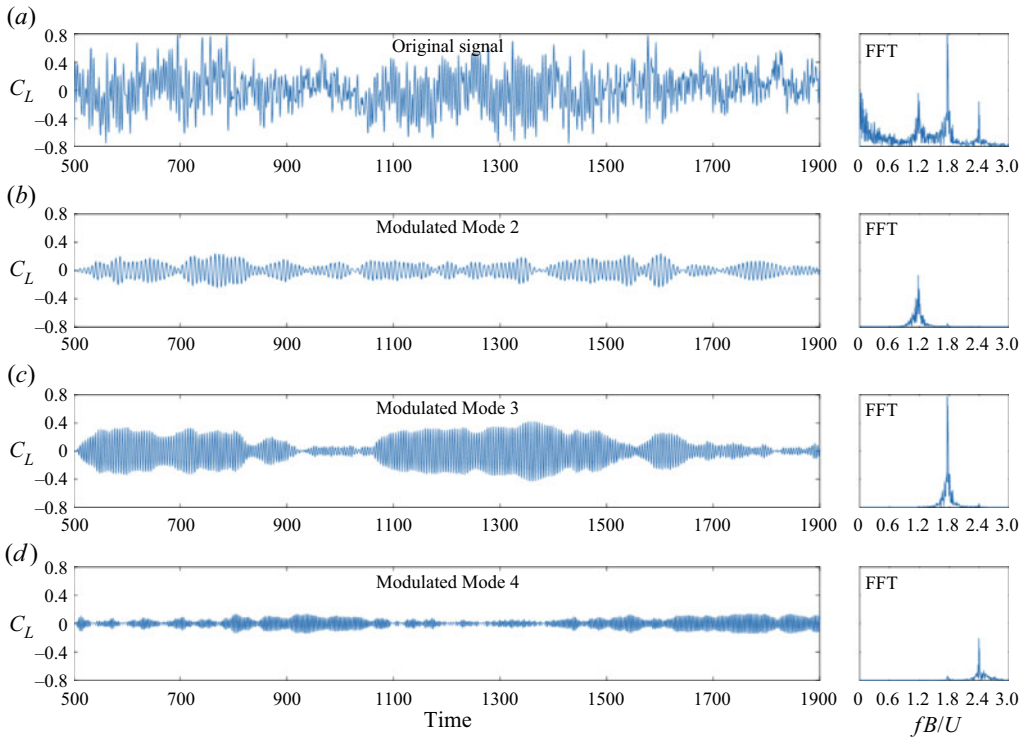
Figure 20. (*a–d*) Band-pass filter for C_L with $B/D = 9$.

mode order. This proportional relationship between the vortex number and the mode order (mode frequency) is highly similar to the Rossiter modes in the cavity flow. Within each mode, the number of *L* vortices is a constant. Therefore, a larger *B/D* means a larger vortex size and wavelength.

(2) In general, the shade of the contour becomes lighter when *B/D* increases from 3 to 9. This is anticipated because the large-scale vortices that are shed from the leading edge break up into more intermittent structures after reattachment. A wider chord means more developed turbulence at the trailing edge, leading to a decrease in the intensity of vortex shedding. Although the number of leading-edge vortices on the lateral sides of the prism increases stepwise with *B/D*, the standard deviation of C_L in figure 22 still shows a decreasing trend as *B/D* increases. This suggests that the intensity of each leading-edge vortex decreases superlinearly with *B/D*. Nevertheless, multiple plateaus in C_L-*std* are observed in figure 19, which are quite well aligned with the mode shifts as *B/D* increases. The reason may be that the trailing-edge vortices are not fully developed at the generation of each new mode (*B/D* = 3, 6, 9 and 12). With the increase in *B/D*, the intensity of trailing-edge vortices increases, negating the reduction in the intensity of the leading-edge vortices.

(3) At the generation of each new mode (*B/D* = 3, 6, 9 and 12), when the new *L* vortex arrives at the trailing edge, the *T* vortex has not been formed yet, and the flow is mainly governed by the ILEV (see, for example, the coherent structures of *B/D* = 6 in figure 10). With an increase in *B/D*, the wavelength of the ILEV tends to be longer, and it needs more time for the *L* vortex to travel from the leading to the
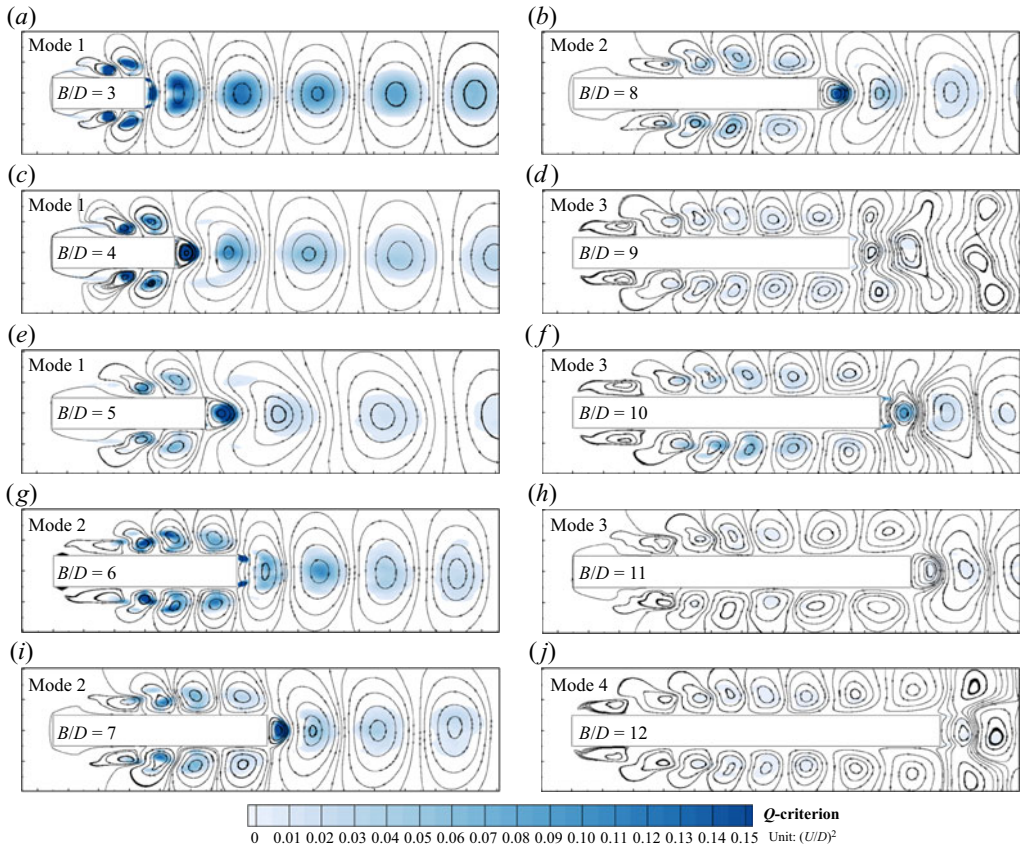
Figure 21. (*a–j*) Streamlines and *Q* contours of the primary *St* mode for different *B/D* values, corresponding to time instant when the lateral clockwise *L* vortices arrive at the trailing edge.

trailing edge, providing an opportunity for the *T* vortex to be better developed. This is reflected by the growth of the size and relative strength of the TEVS. Accordingly, the merging point of the *L* and *T* vortices moves downstream. Since the *L* and *T* vortices can be easily captured by each other in this range, the related instability mode is preferred by the system, making the frequency more concentrated than in other ranges, as shown in figure 18. When *B/D* increases to the upper bound of each mode (*B/D* = 5, 8 and 11), the TEVS is fully developed and begins to shed away when the *L* vortex arrives at the trailing edge, but they can still merge (see the coherent structures for *B/D* = 5 in figure 9). As *B/D* is further increased, the *L* vortex lags far behind the *T* vortex and they cannot capture each other at the trailing edge. Meanwhile, a new *T* vortex, which has an opposite direction of rotation, is formed at the trailing edge, and the original interactions between the *L* and *T* vortices diminish. A more suitable interaction mechanism for the higher-order mode is selected and enhanced by the system, initiating the transition of the global instability from a lower mode to a higher mode.

Based on the above analyses, it can be reaffirmed that the interactions between the ILEV and TEVS are closely related to *B/D* and are responsible for the jump in the main *St* mode. However, this does not necessarily imply that the interference effect of TEVS on the ILEV is the source of the global instability. Figure 23 shows the three prominent DMD
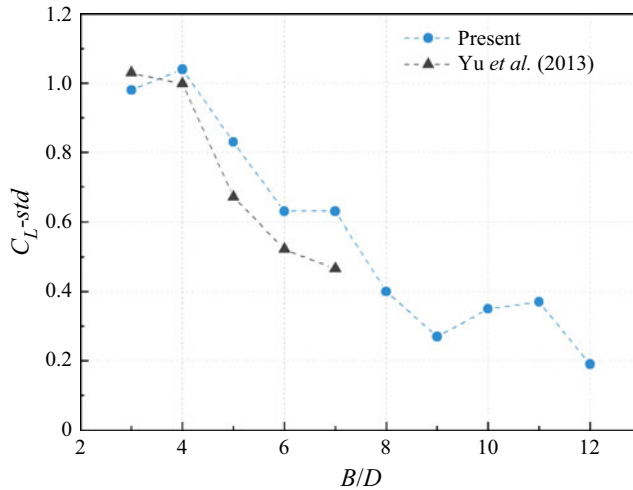
Figure 22. Variation of C_L-std with B/D.

modes in the velocity field for $B/D = 9$, which correspond to Modes 2–4 appearing in the time–frequency spectrum of C_L in figure 19. In Modes 2 and 3, regular TEVS and coalescence with the ILEV are evident. In comparison, the TEVS is almost invisible for Mode 4. The reason for this may be that the frequency of Mode 4 is too high that it exceeds the preferred range of the TEVS. The upper and lower limits of the preferred shedding frequency of the TEVS are discussed in § 6.2. The absence of TEVS for Mode 4 suggests that the instability is not triggered by TEVS but an intrinsic unsteadiness of the separated shear layer, which appears as the ILEV instability. Like the Rossiter modes in cavity flows, multiple shear-layer instability modes may coexist. At a specific B/D, one or two of these modes are captured and enhanced by the TEVS through the interacting mechanism discussed above if their frequencies fall into the preferred range of TEVS. The selection feature of TEVS on the main global instability mode is further demonstrated in § 6.

5.3. *Pressure feedback-loop mechanism*

It has been determined that the global instability is caused by the self-sustained oscillations of the shear layer. Nevertheless, the underlying pressure feedback-loop mechanism related to the self-sustained oscillations remains unclear. To identify this pressure feedback-loop mechanism, the predominant pressure DMD mode at each B/D is extracted from the spanwise-averaged pressure field. The phase distribution of the pressure fluctuations in the flow fields is calculated using (3.10) and is shown in figure 24. The time-averaged streamlines are also presented.

At a specific mode, the number of stagnation points within the chord B is a constant and equals the order of the mode. When B/D is increased from 3 to 5, the wavelength, i.e. the distance between the adjacent stagnation points P_1, P_2, P_3, ... tends to increase. The wavelength then experiences a sudden decrease at $B/D = 6$, accompanied by a jump in the *St* mode. Such a decrease in the wavelength can also be noticed at $B/D = 9$ and 12. At the generation of each new mode ($B/D = 3$, 6, 9 and 12), the phase in the near wake is close to zero. With an increase in B/D, the phase in the near wake increases due to the phase lag between leading-edge vortex shedding and TEVS. Near the mode jump, this phase
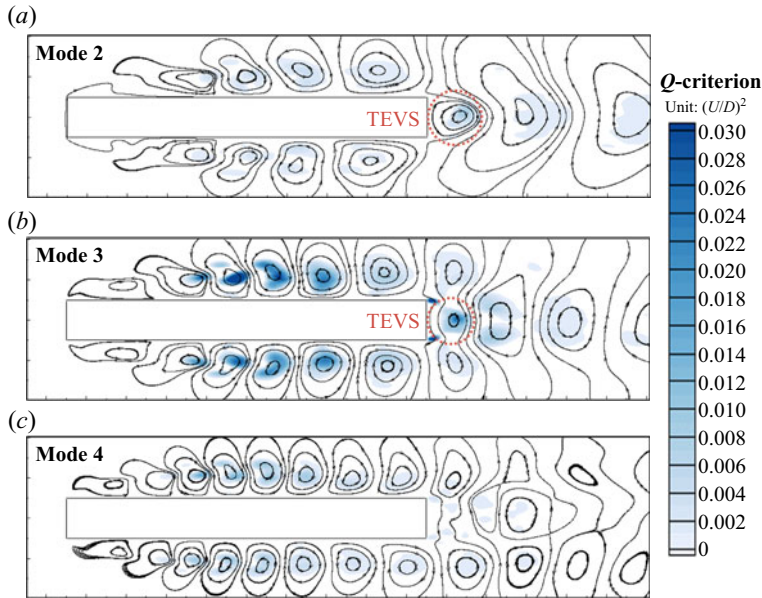
Figure 23. Streamlines and Q contours of (*a*) Mode 2, (*b*) Mode 3 and (*c*) Mode 4 for $B/D = 9$.

lag approaches π for the lower-order mode, while it approaches zero for the higher-order mode. This is in accordance with the discussion above based on the velocity modes in figure 21.

To explore the feedback-loop mechanism of the self-sustained oscillations, the location of the in-phase point P_0 near the trailing edge is determined for each B/D. Unexpectedly, the location of P_0 does not show a uniform pattern for different B/D values. When $B/D = 4$–5, P_0 is located at the upstream region of the trailing edge. For the cases with $B/D = 3$ and $B/D \geq 6$, however, no zero-phase point is observed on the top surface of the prism near the trailing edge. To facilitate the analysis, the contour lines of phase $= 0$ around the trailing edge in these cases are highlighted by red lines.

In the second regime, i.e. $B/D = 3$ and $B/D \geq 6$, the contour line of phase $= 0$ is located immediately behind the T vortex, corresponding to the location of the coalescence of the L and T vortices. This phenomenon confirmed the assumption that the pressure pulse, which is generated by the discontinuity of the boundary when the L vortex passes over the trailing edge, travels upstream to the leading edge. This pressure pulse in turn promotes the merging of the KH rollers at a regular interval and then enhances the self-sustained oscillations of the separated shear layer. Due to the interference effect of the TEVS, the downstream in-phase point is not at the trailing-edge corner but is in the near wake. The more developed the TEVS is, the more the deviation of the phase $= 0$ line from the downstream corner is observed.

When $B/D = 4$–5, P_0 is located at the downstream border of the mean separation bubble, corresponding to the mean reattachment point. It is surmised that some significant changes in the flow characteristics occur when B/D is increased from 5 to 6 and lead to the contrasting feedback-loop mechanisms. Figure 25 shows the evolution of the original flow during one vortex shedding cycle for $B/D = 5$ and 6.

In either case, the reattachment point shows periodical oscillations around the mean reattachment point due to the advection of the L vortices. A distinct difference between the two flows is that the separated shear layer is always reattached to the prism afterbody
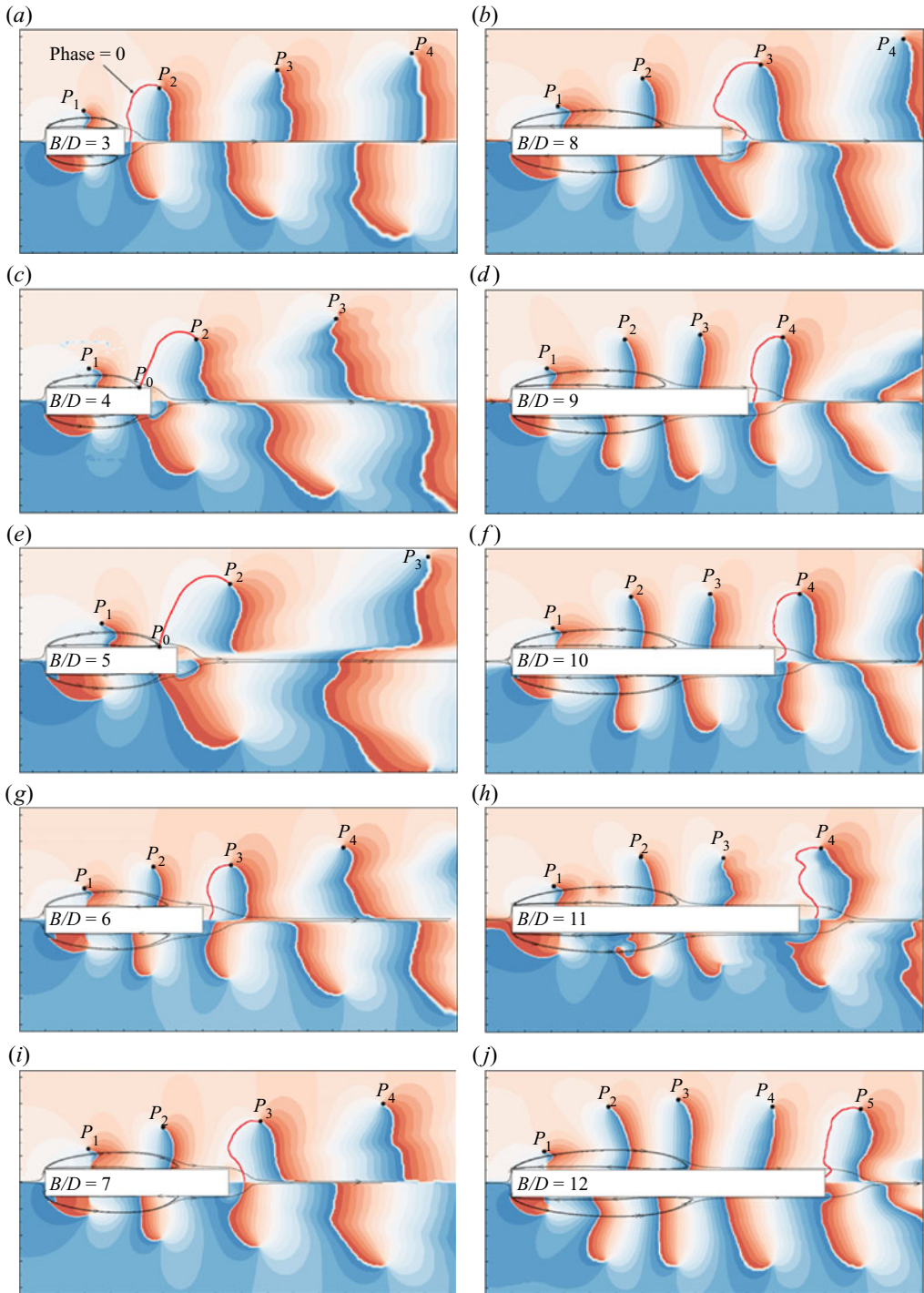
Figure 24. Phase of the pressure fluctuations relative to the upper leading edge in the *St* mode for (*a*–*j*) $B/D = 3$–12.
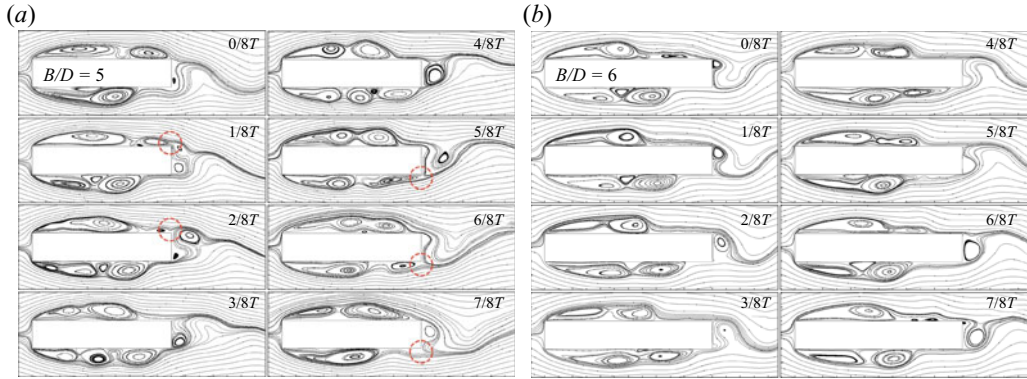
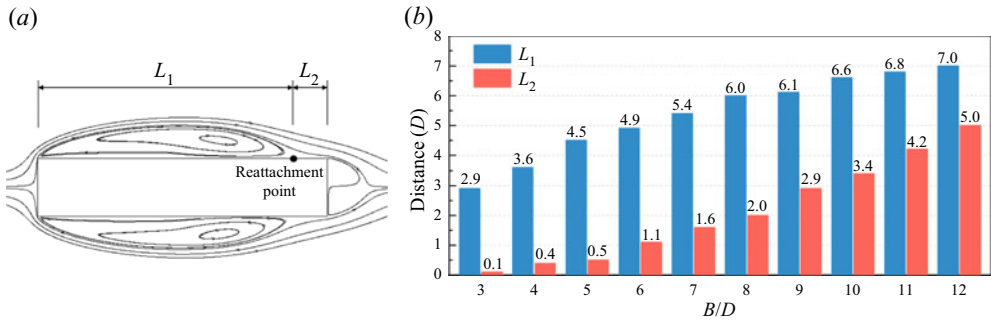Figure 25. Spanwise-averaged streamlines during one period: (*a*) $B/D = 5$; (*b*) $B/D = 6$.

Figure 26. (*a*,*b*) Location of the mean reattachment point for different B/D. Distances L_1 and L_2 denote the distances from the mean reattachment point to the leading and trailing edges, respectively.

for $B/D = 6$, while this is not the case for $B/D = 5$. For $B/D = 5$, the upper and lower shear layers are not reattached to the prism from $T/8$ to $2T/8$ and from $5T/8$ to $7T/8$, respectively, as indicated by the red circles. In other words, the mean reattachment point is too close to the trailing edge (see figure 24) that the transient reattachment point falls outside the side surface temporarily, and the shear layer exhibits an intermittent flapping behaviour on the prism afterbody.

The locations of the mean reattachment point for different B/D values are summarized in figure 26. Kiya & Sasaki (1985) noted that the transient reattachment point fluctuated around the reattachment point in a range of $1D$. When $B/D \leq 5$, the distance from the mean reattachment point to the trailing edge is smaller than $1D$ and thus corresponds to intermittent reattachment. Parker & Welsh (1983) also found this type of switching of the reattachment behaviour at a critical B/D. The intermittent flapping of the shear layer on the prism afterbody at $B/D = 4$ and 5 gives rise to nearly periodic pressure fluctuations, which travel upstream to the leading edge and close the self-sustained oscillation cycle of the shear layer. This feedback loop based on the pressure occurs not over the entire chord length but within the mean separation bubbles.

Based on the different pressure feedback-loop mechanisms, it is surmised that it is more appropriate to refer to the global instabilities at $B/D = 4$–5 and $B/D \geq 6$ as the ISL and the ILEV instabilities, respectively, to reflect the direct source of the upstream-propagating pressure waves. The case of $B/D = 3$ is relatively special because the shear layer is apparently not always reattached to the prism surface, but the pressure phase distribution

955 A19-28

in figure 24 still shows the ILEV instability pattern. Figure 26 shows that the mean reattachment point for $B/D = 3$ is very close to the trailing edge. If the instability of $B/D = 3$ belongs to the ISL instability, P_0 should be almost near the downstream corner. However, there is a weak T vortex near the trailing edge (figure 21), which has a positive relative phase. As a result, the contour line of phase $= 0$ experiences a modulation by the TEVS near the downstream corner, making the global instability appear as the ILEV instability.

For smaller B/D values, such as $B/D = 2$ and 1, the upper and lower separated shear layers are not reattached to the prism surface (Kareem & Cermak 1984; Yu *et al.* 2013) but directly interact with each other in the wake, forming Kármán-type vortex shedding (referred to as the 'leading-edge vortex shedding' regime by Naudascher & Rockwell (1994)). Neither intermittent flapping of the shear layer nor the successive splitting of the large-scale vortices by the sharp downstream corners occurs. Thus, the above-mentioned two instability regimes and the stepwise increase in St cannot be observed in the range of $B/D \leq 2$.

6. Further investigation of the mechanism of global instability

To further validate the pressure feedback-loop mechanism and delineate the contribution of the TEVS to the global instability, flow characteristics of two special geometries (Case II and Case III in figure 1), which are designed to separate the ILEV and TEVS, are investigated in this section.

6.1. *Flow characteristics without TEVS*

The TEVS here mainly refers to Kármán-type vortex shedding. To prevent the formation of Kármán-type vortices, a splitter plate with a width of $5D$ is attached to the middle of the leeward face of the prism of $B/D = 6$. The reason for choosing such a B/D and splitter width is that the separated shear layer was noted to intermittently reattach to the prism surface (not shown here) under this arrangement, and thus the result is more comparable with that of regular prisms of $B/D = 4$–5.

The Strouhal number calculated from the spectrum of C_L is 1.776, corresponding to Mode 3 ($St \approx 0.18$) in figure 17. The corresponding DMD mode is extracted from the spanwise-averaged velocity field, as shown in figure 27. The TEVS is eliminated by the splitter plate, but the regular ILEV is still evident, indicating that TEVS is not a necessity for the global instability. There are three counter-rotating pairs of L vortices on each side of the prism (excluding the splitter plate), which is the same as the mode order. This is consistent with those observed in figure 21 for the regular prisms of Case I.

Figure 28 shows the phase distribution of the pressure St mode. The zero-phase point P_0 again is located at the mean reattachment point, indicating that the global instability in this case is also caused by the pressure feedback loop between the leading edge and the mean reattachment point. From the time-averaged streamline, the distance between the mean reattachment point and the trailing edge is less than $1D$, similar to the cases of $B/D = 4$ and 5, indicating that the shear layers intermittently reattach to the prism afterbody. This behaviour suggests that the global instability is the ISL instability rather than the ILEV instability.

For the regular rectangular cylinder with $B/D = 6$, the L vortices on the lateral sides merge with the T vortex in the near wake, and the width of vortices in the wake is relatively large. For Case II, however, the splitter plate eliminates the TEVS and prohibits the L vortices on the two sides from merging together, and thus the vortex width is smaller.
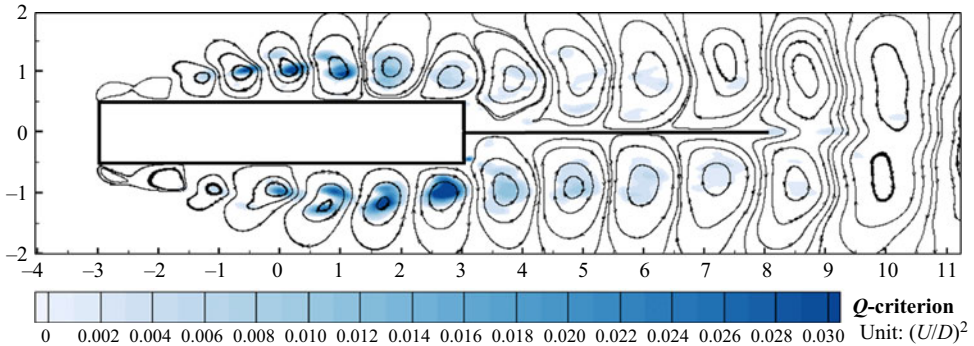
Figure 27. Streamlines and Q contours of the St mode for Case II.
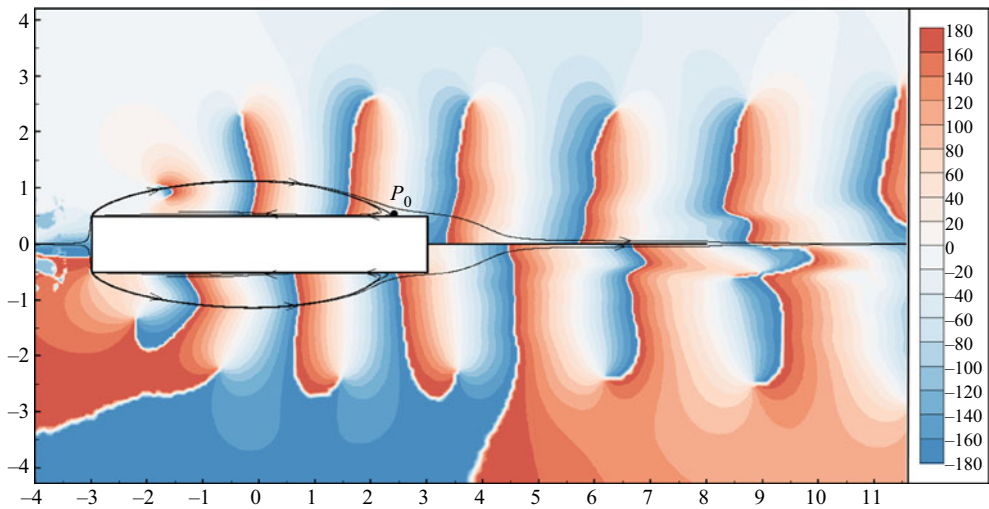

Figure 28. Phase of the pressure fluctuations relative to the upper leading edge in the St mode for Case II.

For a fixed convection velocity, a shorter vortex width means a higher shedding frequency. In addition, without the interference effect of the TEVS, the ILEV can select its preferred shedding frequency. As a result, Case II with a splitter plate could reach a higher St number and DMD mode.

The above analysis shows that the formation of the self-sustained oscillations of the separated shear layer is independent of the TEVS. However, C_L-std of the integral structure (prism and splitter plate) is 0.14, much smaller than 0.37 of the regular prism with $B/D = 11$, which has the same total width. In addition, Nakamura & Nakashima (1986) found that the flows over H-section prisms with and without a splitter plate both suggest the presence of the ISL instability, while the vortex shedding on the two sides with the splitter plate are not antiphase but rather in phase. Thus, although the TEVS is not essential for the global instability, its participation may influence the global instability significantly.

6.2. *Flow characteristics without ILEV*

To better investigate the source and behaviour of the TEVS, the separated shear layer is excluded by extending the prism lateral faces upstream to the inlet boundary, as depicted
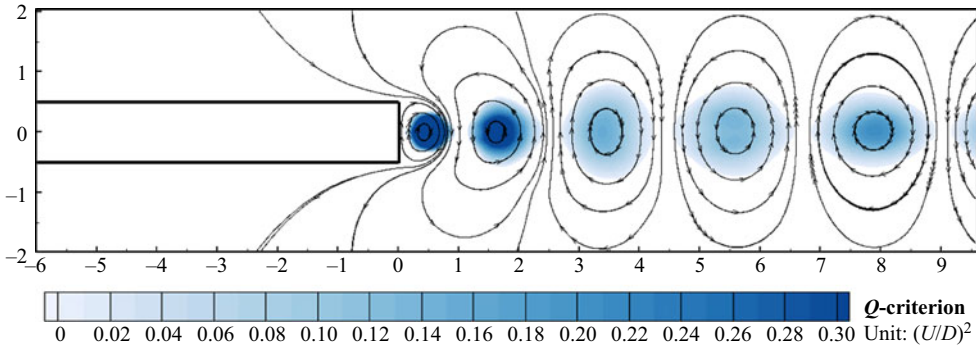
955 A19-30

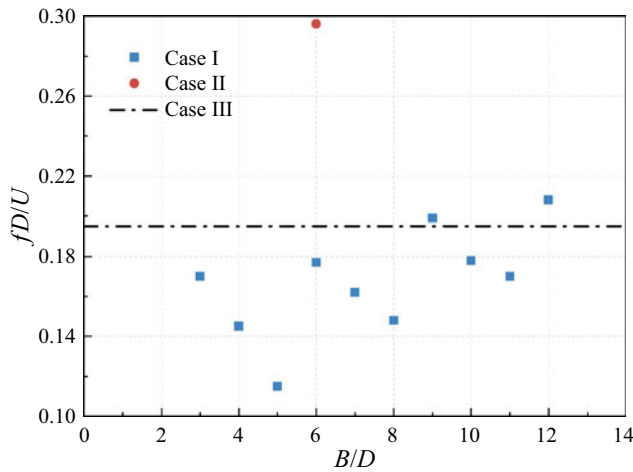Figure 29. Streamlines and Q contours of the St mode for Case III.

Figure 30. Strouhal number (based on D) for different B/D ratios.

in figure 1. Since the prism width in this case has no direct meaning, St is calculated based on D and is 0.195. The corresponding instability mode is shown in figure 29. A regular Kármán vortex street is formed in the wake as a result of the interactions between the upper and lower shear layers separated at the trailing edge.

Combined with the evolution of the coherent structures in figure 9 and the instantaneous streamlines in figure 25, it can be confirmed that the TEVS in the global instability of the rectangular prisms is caused by the intermittent shear layers in the interval of two neighbouring ILEVs. A larger ILEV wavelength leads to a wider boundary layer and further a more developed TEVS. This relationship can be ascertained by the DMD mode shapes of different B/D values in figure 21.

If St of the regular rectangular prisms (Case I) is calculated based on D, it is noted to be distributed within the range of 0.11–0.21, as shown in figure 30. This range is often described as the preferred shedding frequency of TEVS (Mills *et al.* 2002, 2003). The $St(D)$ experiences a monotonic decrease with B/D within each mode, but shows a sudden increase around the mode jump.

Now, the influence of TEVS on the global instability in Case I can be determined. On the one hand, for the global instability to be formed, the shedding frequencies of the ILEV and the TEVS should be the same. The shedding frequency of the T vortex is controlled

by the convective velocity of the shear layer U_b. The value of U_b is usually smaller than the free-stream velocity of Case III, and thus the TEVS frequency should be smaller than that of Case III (0.195). As shown in figure 30, most of the $St(D)$ values of Case I are smaller than 0.195. This forms the upper limit of the frequency of the global instability. For $B/D = 9$ and 12, St of the main instability mode is close to the upper limit, making the ILEV and TEVS less compatible. As a consequence, the main instability mode is less enhanced, and the spectrum becomes more complicated compared with adjacent B/D values, as shown in figure 18. On the other hand, the lower limit of St is achieved through the length of the shear layer. If St is too low, the shear layer between two L vortices is long enough for the T vortex to fully develop and shed from the trailing edge before the arrival of the L vortices. As a result, the L and T vortices cannot capture each other, and the original instability mode cannot be maintained, as discussed in § 5.2.

Due to the above limitations imposed by the TEVS, only the most suitable modes, whose frequencies fall into the preferred range of TEVS, will be selected and enhanced by the system for each B/D. For Case II, however, the TEVS is removed and the system can reselect its preferred frequency based on the ILEV. Thus, St of Case II is much higher than that of Case III. It is worth mentioning that the TEVS decides which instability mode should be selected, but it does not directly change the frequency of a specific mode. The mode frequency is governed by the pressure feedback-loop mechanism and is characterized by an integral multiple of 0.6 (based on B).

7. Concluding remarks

Based on the large-eddy simulation and analysis employing DMD, the behaviour and mechanism of the global instability are investigated for prisms with a wide range of chord-to-depth ratios (B/D) at $Re = 1000$.

The interaction between the ILEV shedding and TEVS and its variation with B/D are recognized based on the velocity DMD mode. The leading- and trailing-edge vortices merge together in the near wake, and the level of development of trailing-edge vortices is dependent on B/D. Due to the integral number of leading-edge vortex pairs on the side of the body and the interference effect of TEVS, St based on B shows a stepwise variation with the change of B/D. Within each mode, the phase difference between the TEVS and ILEV at the trailing edge increases with B/D until it reaches π, thus promoting the transition from the lower mode to the higher mode.

Two types of pressure feedback mechanism controlling the global instability are revealed based on the phase distribution in the pressure DMD mode. When $B/D = 4$ and 5, the shear layer is intermittently reattached to the prism afterbody and exhibits a flapping behaviour. Thus, the flow is characterized by the ISL instability and the feedback loop covers the separation region. When $B/D \geq 6$, however, the shear layer is fully reattached to the prism. The shear-layer instability is enhanced by the upstream propagation of the pressure pulse induced by the discontinuity of the boundary condition and the interference effect of trailing-edge vortices when the leading-edge vortices flow past the trailing edge. Thus, the flow is characterized by the ILEV instability, and the feedback loop covers the entire chord. For $B/D = 3$, due to the mean reattachment point being very close to the trailing edge, the flow still shows the ILEV instability under the interference effect of the TEVS.

Based on an additional case with a splitter plate, it is found that the ILEV can reach a much higher frequency without the participation of TEVS. According to St (based on D) of regular rectangular prisms, the preferred shedding frequency of the TEVS is determined. Based on an additional case where the leading-edge vortices are removed, it is found that the lower and upper limits of the preferred shedding frequency are governed by the phase

difference between ILEV and TEVS and the convective velocity of the separated shear layer at the trailing edge, respectively. Due to the interaction between the ILEV and TEVS, only the most suitable ILEV modes whose frequencies fall into the preferred range of TEVS will be selected and enhanced by the system for each *B/D*, leading to the stepwise increase in *St* with *B/D*.

Declaration of interests. The authors report no conflict of interest.

Author ORCIDs.

Fuyou Xu http://orcid.org/0000-0002-5497-5378;

Hongyi Jiang http://orcid.org/0000-0002-0137-6355.

REFERENCES

BASLEY, J., PASTUR, L.R., DELPRAT, N. & LUSSEYRAN, F. 2013 Space-time aspects of a three-dimensional multi-modulated open cavity flow. *Phys. Fluids* **25** (6), 064105.

BRES, G.A. & COLONIUS, T. 2008 Three-dimensional instabilities in compressible flow over open cavities. *J. Fluid Mech.* **599**, 309–339.

BRUNO, L., COSTE, N. & FRANSOS, D. 2012 Simulated flow around a rectangular 5: 1 cylinder: Spanwise discretisation effects and emerging flow features. *J. Wind Engng Ind. Aerodyn.* **104**, 203–215.

CESUR, A., CARLSSON, C., FEYMARK, A., FUCHS, L. & REVSTEDT, J. 2014 Analysis of the wake dynamics of stiff and flexible cantilever beams using POD and DMD. *Comput. Fluids* **101**, 27–41.

CHAURASIA, H.K. & THOMPSON, M.C. 2011 Three-dimensional instabilities in the boundary-layer flow over a long rectangular plate. *J. Fluid Mech.* **681**, 411–433.

CIMARELLI, A., LEONFORTE, A. & ANGELI, D. 2018 On the structure of the self-sustaining cycle in separating and reattaching flows. *J. Fluid Mech.* **857**, 907–936.

DUAN, G., LAIMA, S., CHEN, W. & LI, H. 2020 Effects of leading-edge separation on the vortex shedding and aerodynamic characteristics of an elongated bluff body. *J. Wind Engng Ind. Aerodyn.* **206**, 104356.

GUÉNIAT, F., PASTUR, L. & LUSSEYRAN, F. 2014 Investigating mode competition and three-dimensional features from two-dimensional velocity fields in an open cavity flow by modal decompositions. *Phys. Fluids* **26** (8), 085101.

HOURIGAN, K., MILLS, R., THOMPSON, M.C., SHERIDAN, J., DILIN, P. & WELSH, M.C. 1993 Base pressure coefficients for flows around rectangular plates. *J. Wind Engng Ind. Aerodyn.* **49** (1–3), 311–318.

HOURIGAN, K., THOMPSON, M.C. & TAN, B.T. 2001 Self-sustained oscillations in flows around long blunt plates. *J. Fluids Struct.* **15** (3–4), 387–398.

HWANG, K.S., SUNG, H.J. & HYUN, J.M. 2000 Visualizations of large-scale vortices in flow about a blunt-faced flat plate. *Exp. Fluids* **29** (2), 198–201.

KAREEM, A. & CERMAK, J.E. 1984 Pressure fluctuations on a square building model in boundary-layer flows. *J. Wind Engng Ind. Aerodyn.* **16** (1), 17–41.

KEGERISE, M.A., SPINA, E.F., GARG, S. & CATTAFESTA, L.N. III 2004 Mode-switching and nonlinear effects in compressible flow over a cavity. *Phys. Fluids* **16** (3), 678–687.

KIJEWSKI, T. & KAREEM, A. 2003 Wavelet transforms for system identification in civil engineering. *Comput.-Aided Civil Infrastruct. Engng* **18** (5), 339–355.

KIYA, M. & SASAKI, K. 1985 Structure of large-scale vortices and unsteady reverse flow in the reattaching zone of a turbulent separation bubble. *J. Fluid Mech.* **154**, 463–491.

LI, X., LYU, Z., KOU, J. & ZHANG, W. 2019 Mode competition in galloping of a square cylinder at low Reynolds number. *J. Fluid Mech.* **867**, 516–555.

LUO, X. & KAREEM, A. 2021 Dynamic mode decomposition of random pressure fields over bluff bodies. *J. Engng Mech. ASCE* **147** (4), 04021007.

LUSSEYRAN, F., PASTUR, L. & LETELLIER, C. 2008 Dynamical analysis of an intermittency in an open cavity flow. *Phys. Fluids* **20** (11), 114101.

MEZIĆ, I. 2013 Analysis of fluid flows via spectral properties of the Koopman operator. *Annu. Rev. Fluid Mech.* **45**, 357–378.

MILLS, R., SHERIDAN, J. & HOURIGAN, K. 2002 Response of base suction and vortex shedding from rectangular prisms to transverse forcing. *J. Fluid Mech.* **461**, 25–49.

MILLS, R., SHERIDAN, J. & HOURIGAN, K. 2003 Particle image velocimetry and visualization of natural and forced flow around rectangular cylinders. *J. Fluid Mech.* **478**, 299–323.

MURRAY, N.E. & UKEILEY, L.S. 2007 Modified quadratic stochastic estimation of resonating subsonic cavity flow. *J. Turbul.* **8**, N53.

NAKAMURA, Y., OHYA, Y. & TSURUTA, H. 1991 Experiments on vortex shedding from flat plates with square leading and trailing edges. *J. Fluid Mech.* **222**, 437–447.

NAKAMURA, Y., OHYA, Y., OZONO, S. & NAKAYAMA, R. 1996 Experimental and numerical analysis of vortex shedding from elongated rectangular cylinders at low Reynolds numbers 200-103. *J. Wind Engng Ind. Aerodyn.* **65** (1-3), 301–308.

NAKAMURA, Y. & NAKASHIMA, M. 1986 Vortex excitation of prisms with elongated rectangular, H and ⊢ cross-sections. *J. Fluid Mech.* **163**, 149–169.

NAUDASCHER, E. & ROCKWELL, D. 1994 *Flow-Induced Vibrations: An Engineering Guide*. AA Balkema.

NGUYEN, D.T., HARGREAVES, D.M. & OWEN, J.S. 2018 Vortex-induced vibration of a 5:1 rectangular cylinder: a comparison of wind tunnel sectional model tests and computational simulations. *J. Wind Engng Ind. Aerodyn.* **175**, 1–16.

OHYA, Y., NAKAMURA, Y., OZONO, S., TSURUTA, H. & NAKAYAMA, R. 1992 A numerical study of vortex shedding from flat plates with square leading and trailing edges. *J. Fluid Mech.* **236**, 445–460.

OKAJIMA, A. 1982 Strouhal numbers of rectangular cylinders. *J. Fluid Mech.* **123**, 379–398.

PARKER, R. & WELSH, M.C. 1983 Effects of sound on flow separation from blunt flat plates. *Intl J. Heat Fluid Flow* **4** (2), 113–127.

PASTUR, L.R., LUSSEYRAN, F., FAURE, T.M., FRAIGNEAU, Y., PETHIEU, R. & DEBESSE, P. 2008 Quantifying the nonlinear mode competition in the flow over an open cavity at medium Reynolds number. *Exp. Fluids* **44** (4), 597–608.

PRASAD, A. & WILLIAMSON, C.H. 1997 The instability of the shear layer separating from a bluff body. *J. Fluid Mech.* **333**, 375–402.

ROCKWELL, D. & NAUDASCHER, E. 1978 Review–self-sustaining oscillations of flow past cavities. *J. Fluids Engng* **100**, 152–165.

ROWLEY, C.W., MEZIĆ, I., BAGHERI, S., SCHLATTER, P. & HENNINGSON, D.S. 2009 Spectral analysis of nonlinear flows. *J. Fluid Mech.* **641**, 115–127.

SAMPATH, R. & CHAKRAVARTHY, S.R. 2014 Proper orthogonal and dynamic mode decompositions of time-resolved PIV of confined backward-facing step flow. *Exp. Fluids* **55** (9), 1792.

SASAKI, K. & KIYA, M. 1991 Three-dimensional vortex structure in a leading-edge separation bubble at moderate Reynolds numbers. *J. Fluids Engng* **113**, 405–410.

SCHMID, P.J. 2010 Dynamic mode decomposition of numerical and experimental data. *J. Fluid Mech.* **656**, 5–28.

SEENA, A. & SUNG, H.J. 2011 Dynamic mode decomposition of turbulent cavity flows for self-sustained oscillations. *Intl J. Heat Fluid Flow* **32** (6), 1098–1110.

STANKIEWICZ, W., MORZYŃSKI, M., KOTECKI, K., ROSZAK, R. & NOWAK, M. 2016 Modal decomposition-based global stability analysis for reduced order modeling of 2D and 3D wake flows. *Intl J. Numer Meth. Fluids* **81** (3), 178–191.

STOKES, A.N. & WELSH, M.C. 1986 Flow-resonant sound interaction in a duct containing a plate, II: Square leading edge. *J. Sound Vib.* **104** (1), 55–73.

TAN, B.T., THOMPSON, M.C. & HOURIGAN, K. 2004 Flow past rectangular cylinders: receptivity to transverse forcing. *J. Fluid Mech.* **515**, 33–62.

THOMPSON, M.C., RADI, A., RAO, A., SHERIDAN, J. & HOURIGAN, K. 2014 Low-Reynolds-number wakes of elliptical cylinders: from the circular cylinder to the normal flat plate. *J. Fluid Mech.* **751**, 570–600.

TU, J.H., ROWLEY, C.W., LUCHTENBURG, D.M., BRUNTON, S.L. & KUTZ, J.N. 2013 On dynamic mode decomposition: theory and applications. arXiv:1312.0041.

WILLIAMSON, C.H.K. 1988 The existence of two stages in the transition to three-dimensionality of a cylinder wake. *Phys. Fluids* **31** (11), 3165–3168.

YALLA, S.K. & KAREEM, A. 2001 Beat phenomenon in combined structure-liquid damper systems. *Engng Struct.* **23** (6), 622–630.

YOSHIZAWA, A. 1986 Statistical theory for compressible turbulent shear flows, with the application to subgrid modeling. *Phys. Fluids* **29** (7), 2152–2164.

YU, D., BUTLER, K., KAREEM, A., GLIMM, J. & SUN, J. 2013 Simulation of the influence of aspect ratio on the aerodynamics of rectangular prisms. *J. Engng Mech. ASCE* **139** (4), 429–438.

ZHANG, Q., LIU, Y. & WANG, S. 2014 The identification of coherent structures using proper orthogonal decomposition and dynamic mode decomposition. *J. Fluids Struct.* **49**, 53–72.

ZHANG, Z. & XU, F. 2020 Spanwise length and mesh resolution effects on simulated flow around a 5:1 rectangular cylinder. *J. Wind Engng Ind. Aerodyn.* **202**, 104186.

ZHAO, J., HOURIGAN, K. & THOMPSON, M.C. 2018 Flow-induced vibration of D-section cylinders: an afterbody is not essential for vortex-induced vibration. *J. Fluid Mech.* **851**, 317–343.